Rep. Prog. Phys. **72** (2009) 122501 (26pp) doi:10.1088/0034-4885/72/12/122501

Theory of radio frequency spectroscopy experiments in ultracold Fermi gases and their relation to photoemission in the cuprates

Qijin Chen[1,2], **Yan He**[1], **Chih-Chun Chien**[1] **and K Levin**[1]

[1] James Franck Institute and Department of Physics, University of Chicago, Chicago, IL 60637, USA
[2] Zhejiang Institute of Modern Physics and Department of Physics, Zhejiang University, Hangzhou, Zhejiang 310027, People's Republic of China

Received 3 March 2009
Published 22 October 2009
Online at stacks.iop.org/RoPP/72/122501

Abstract

In this paper we present an overview of radio frequency (RF) spectroscopy in the atomic Fermi superfluids with the ultimate goal of suggesting new directions in the cold gas research agenda from the condensed matter perspective. We review the experimental and theoretical literature on cold gases and the photoemission spectroscopy of the cuprates particularly as it pertains to areas of overlap. In addition to a comparison with the cuprates, this paper contains a systematic overview of the theory of RF spectroscopy, both momentum integrated and momentum resolved. It should be noted that the integrated and momentum resolved forms of photoemission are equally important in the high T_c cuprate literature. For the cold gases we introduce the reader to such topical issues as the effects of traps, population imbalance, final state interactions and, over the entire range of temperatures, we compare theory and experiment. We show that this broad range of phenomena can be accommodated within the BCS-Leggett description of BCS–BEC crossover. Importantly, this scheme captures some of the central observations in photoemission experiments in the cuprates.

(Some figures in this article are in colour only in the electronic version)

This article was invited by Professor L Greene.

Contents

1. Introduction

There is considerable excitement surrounding the discovery [1–10] of superfluidity in the ultracold Fermi gases. What is novel about these new superfluids is that using a Feshbach resonance [11] one can tune the attractive interaction from weak (as in the BCS limit) to strong as in the Bose Einstein condensation (BEC) regime. We note that BCS theory is, in many ways, the paradigm of condensed matter theories. Thus, the fact that an entire body of work on conventional superconductors has concentrated on a very special case of a much more general phenomenon underlines the importance of these cold Fermi gases [12, 13]; they provide a unique opportunity for elucidating a very powerful generalization of BCS theory. In addition, a number of people [14–18] have also argued that this BCS–BEC crossover might be relevant to the cuprate superconductors. In this way we see that the tunability of the interaction strength in the Fermi gases can yield a possible simulation of key aspects of the high temperature superconductors.

In large part the rationale for application of BCS–BEC crossover to the cuprates derives from their anomalously short coherence length [19]. However, additional arguments [14] in support of this scenario come from the fact that T_c is anomalously high so that the attractive interaction driving the superconducting pairing may be stronger than that associated with strict BCS theory. In addition, the cuprates are quasi-two-dimensional so that the onset of superconductivity is expected to be relatively continuous; this leads to the notion that there is some degree of pairing in the normal state as is consistent with the crossover picture. In a related vein, perhaps most interesting about the BCS–BEC crossover scenario for the cuprates is that it leads naturally to 'pseudogap' effects, that is a pairing gap which sets in smoothly at T^*, above T_c. Of all issues currently studied in the field of high temperature superconductors, the question of the origin of the pseudogap has attracted the most attention. Is this pseudogap related to the superconductivity itself, as in the crossover approach, or does it reflect a hidden additional order parameter?

Theories of the cuprates which are based on the notion that the pseudogap has something to do with the superconductivity comprise a rather large class of approaches [20–22], of which the crossover scenario is only one. This latter scenario is to be distinguished from the so-called 'phase fluctuation' scheme [20]. It is is argued that the low plasma frequency associated with the underlying parent insulating state leads to an exotic normal state in which there are correlated regions of pairing amplitude without phase coherence. By contrast, the BCS–BEC crossover approach builds on the stronger-than-BCS attractive interaction associated with the short coherence length. Here one has 'pairing fluctuations' or pre-formed pairs in the normal state. Importantly, as one goes below T_c these pairs persist as non-condensed pair excitations [23] of the condensate. This leads to a gentler onset of superfluid coherence, with progressively more pairs falling into the condensed state as T is decreased below T_c. We will see that, as a consequence, the crossover approach helps to reconcile some otherwise paradoxical experiments which have been interpreted to suggest a 'two-gap' picture [18] for a range of photoemission and other phenomena. The two gaps here would then correspond to the contribution from the non-condensed and condensed pairs.

As compared with the pseudogap, rather less attention in the cuprate field has been focused on the nature of the attractive interaction which is responsible for high T_c superconductivity, although it is generally believed that in one sense or another this is to be associated with the underlying physics of the Mott insulating parent compound. Indeed, the crossover scenario begs the question of the pairing mechanism and simply assumes that there is an attractive interaction of unknown but arbitrary strength. Since, in this approach, the pseudogap onset temperature is identified with the pairing onset, and since T^* increases as the insulator is approached, it is quite likely that 'Mott physics' in one form or another is, indeed, responsible for the pairing. From a very different perspective, it has also been argued that future cold gas experiments on optical lattices [24] will provide a simulation of repulsive Hubbard models, which might further elucidate the nature of the pairing interaction and of 'Mott physics' aspects [22] of high T_c superconductivity. This would be most relevant if, indeed, the repulsive Hubbard model is the source of an attraction in the d-wave channel.

While condensed matter physicists have a wealth of well-developed techniques for characterizing electronic superconductors, the tools currently available to the atomic physicists who study the Fermi gases are more limited. Moreover, in these gases, it is not at all straightforward to determine something as commonplace as the temperature in the gas, although some impressive progress [8, 25, 26] has been made along these lines. This paper is devoted to addressing one of the most powerful techniques currently being applied to the Fermi gases: radio frequency (RF) spectroscopy. We will show how this technique is similar to that of photoemission in condensed matter physics and exploit the analogy, already discussed in the literature [27], between momentum resolved RF and angle resolved photoemission spectroscopy (ARPES). As a background for both communities, we review some of the experimental and theoretical literature on RF spectroscopy (of cold gases) and photoemission spectroscopy (of the cuprates).

We argue that there are a number of issues which have been central to high temperature superconductivity which would be useful to address more systematically in the ultracold Fermi gases. Perhaps the most notable example of commonality [14, 15] in this regard is the ubiquitous pseudogap phase.

We will see that photoemission experiments [28, 29] in the cuprates and RF spectroscopy in the atomic Fermi gases both depend on the important fermionic spectral function $A(\boldsymbol{k}, \omega)$ which characterizes completely the single fermion or one-particle properties of a given many body system. In simplistic terms, the driving force motivating the photoemission studies in the cuprates is to acquire an understanding of the 'mechanisms' and nature of high T_c superconductivity. There has been a recent emphasis on high temperatures near T^*, where the pseudogap turns on and on the region from slightly above to somewhat below the superfluid transition temperature, T_c. By contrast in the ultracold gases, the RF spectra have been studied in the hopes of characterizing the pairing gap Δ—much like tunneling is used in conventional superconductors. There has been a recent emphasis on very low temperatures $T \ll T_c$ and in particular on quantifying the size of Δ at $T = 0$.

Some of the key issues that have emerged in photoemission studies of the cuprates involve (i) a characterization of the self-energy contained in the spectral function. Different empirical models [30] have been deduced which, it is argued, might ultimately hold the clue to the nature of the mediating boson. (ii) Also important is the origin of the pseudogap [14, 22] and whether this gap is a signature of a hidden order parameter or whether it reflects the incipient pairing which ultimately leads to the condensed phase at lower T. (iii) It is viewed as extremely important to arrive at an understanding of how superconducting coherence manifests itself in these spectroscopic experiments as one goes from the normal to the ordered phase. This is a complicated question, given the presence of a normal state (pseudo)gap. Finally, other issues of interest are the nature of the order parameter and pseudogap symmetry (which have been shown to be consistent with d-wave). Indeed, in the cuprates this d-wave symmetry has led to a complexity not anticipated in the s-wave Fermi gases associated with (iv) the contrasting T dependent behavior of photoemission (and other properties) near the gap nodes as compared with that near the gap maxima or anti-nodes.

In the cold gases an underlying goal has been to test different theories of BCS–BEC crossover, particularly establishing the most suitable ground state and its quantitative implications such as the pair size [31]. The parameters which quantify the nature of the scale-free or 'unitary' gas have also been addressed. Of additional interest are studies on how population imbalance [32–35] can co-exist with superfluidity. Here new phases associated with, for example, the exotic [36] Larkin–Ovchinnikov–Fulde-Ferrell (LOFF) form of pairing have been contemplated. Even more topical is the behavior in the limit of extreme imbalance [34, 35].

One can see that, despite the similarities in these two spectroscopic techniques, the research agenda in the two communities is rather different. In the high temperature superconductors, the focus has been on the temperature regime near T_c. Furthermore, quantitative issues are viewed as of considerably less importance than arriving at a qualitative understanding, which is still very incomplete. By contrast, in the ultracold Fermi gases the focus has been on temperatures associated with the ground state and on arriving at a more complete quantitative characterization. This brings us to a major goal of this paper, which is to suggest new directions in the cold gas research agenda from the condensed matter perspective. In particular, we wish to highlight differences and similarities in the cold gases with the analogous cuprate studies. A general theme, which takes a cue from the copper oxide superconductors, is to focus on a characterization of (i) the fermionic self-energy, (ii) the pseudogap phase and (iii) how superfluid coherence is established and manifested (in these spectroscopies) at and below T_c.

2. Motivation and background

2.1. Comparing and contrasting RF with photoemission

Photoemission and angle resolved photoemission spectroscopy (ARPES) have been remarkable tools for characterizing cuprate superconductors [28, 29]. Here one invokes the 'sudden' approximation which corresponds to the assumption that the electron acquires the photon energy instantaneously and emerges from the crystal surface immediately. As a consequence, photoemission is associated with electrons near the crystal surface. In addition, only the momentum component in parallel with the surface is conserved. It follows that ARPES is ideal for layered materials. The energy levels involved in the ARPES process are shown in the left panel of figure 1. Here, and throughout the paper, we define the quantity E_k corresponding to the dispersion of the paired fermions in terms of the usual BCS expression

$$E_k \equiv \sqrt{(\epsilon_k - \mu)^2 + \Delta^2(T)}. \tag{1}$$

Because of the large photon energy $h\nu$, compared with the electron energy scale inside the crystal, the final state of the photo-emitted electron is essentially free so that the energy conservation constraint is given by $E_i = E_f - h\nu$, where $E_f = \boldsymbol{k}^2/2m_e$ is measured with an energy analyzer. Here m_e denotes the electron mass. In turn, the momentum (in the known direction) has magnitude $k = \sqrt{2m_e E_f}$. The ARPES spectrum is given by [28]

$$I^{\text{photo}}(\boldsymbol{k}, \omega) = M_0(\boldsymbol{k}, \nu) A(\boldsymbol{k}, \omega) f(\omega), \tag{2}$$

where $M_0(\boldsymbol{k}, \nu)$ is a matrix element which depends on the photon energy. Apart from the matrix element and the Fermi function $f(\omega)$, one sees that ARPES measures the electronic spectral function.

The energy levels involved in an RF transition are shown in the right panel of figure 1. Here Ω_L is the RF frequency for exciting a free atom from hyperfine level 2 (labeled 'free') to level 3 (labeled 'final'). We neglect final state effects, which will be discussed later. A significant difference between an RF and ARPES transition is that in the RF case a dominantly large fraction (Ω_L) of the photon energy is converted to excite a

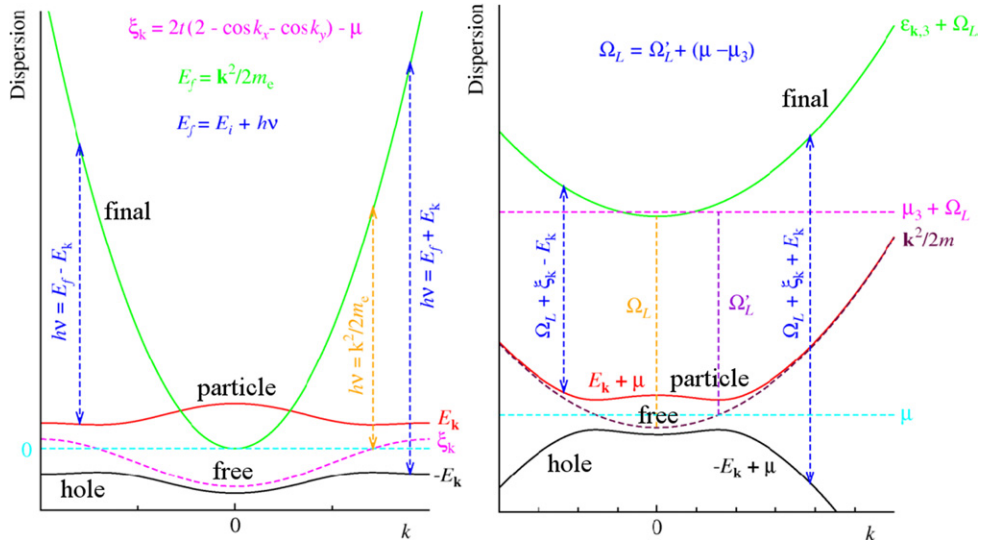

Figure 1. Figure on left: energy levels in an ARPES transition. In a paired system there are two fermionic states which contribute to the photoemitted current. These curves are labeled 'particle' and 'hole'. The upper branch ('particle') will not be occupied until the temperature is high. Here a tight binding dispersion $\xi_k \equiv \epsilon_k - \mu$ is assumed for the underlying non-paired initial state (labeled 'free'). The lower horizontal dashed line indicates the Fermi level of the electrons and the solid line labeled 'final' the dispersion of outgoing electrons. Figure on right: energy levels in an RF transition. Ω_L is the RF frequency for exciting a free atom from hyperfine level 2 (labeled 'free') to level 3 (labeled 'final'). Ω'_L is the same energy but measured relative to the respective chemical potentials. The curves labeled 'particle' and 'hole' are the dispersion of the particle and hole branch of a paired atom in level 2, with energy level given by $\pm E_k + \mu$, respectively. (Color online.)

fermion from one internal state to another. As a consequence, the excited atoms do not have a substantially higher kinetic energy so that they do not leave the bulk gas immediately after the transition until they are deliberately released. The energy zero for an RF transition is more conveniently chosen to be the bottom of the free atom band of state 2. In this convention, the final state energy is $E_f = \Omega_L + \epsilon_k$, where $\epsilon_k = k^2/2m$, and the initial state energy is $E_i = \pm E_k + \mu$ for the two branches shown in figure 1 (right panel) so that $h\nu = E_f - E_i$.

The RF current (which will be derived in section 3.3) is

$$I_0^{RF}(\nu) = \sum_{\boldsymbol{k}} I_0^{RF}(\boldsymbol{k}, \nu) = \sum_{\boldsymbol{k}} \frac{|T_k|^2}{2\pi} A(\boldsymbol{k}, \omega) f(\omega)\Big|_{\omega=\xi_k-\nu}, \quad (3)$$

where $|T_k|^2$ is a tunneling matrix element and it should be noted that there is the restriction $\omega = \xi_k - \nu$ which (apart from matrix element effects) serves to differentiate the photoemission and RF responses.

Finally, the momentum resolved RF experiments to which we frequently refer to effectively measure [27] the 'occupied spectral intensity', much like photoemission, which corresponds to

$$A(k, \omega) f(\omega) k^2/2\pi^2, \quad (4)$$

where the angular degrees of freedom have been integrated out. In a related fashion, we draw attention to earlier suggestions [37] that stimulated Raman spectroscopy in the cold gases can be used as an alternative analog probe to photoemission studies in the cuprates.

2.2. *Overview of the literature on RF experiments*

Experiments and theory have worked well hand in hand in developing an understanding of the so-called 'RF pairing gap spectroscopy' in the atomic Fermi gases. This class of experiments was originally suggested by Torma and Zoller and their colleagues [38, 39] as a method for establishing the presence of superfluidity. In this context an equation equivalent to equation (3) was derived. Later work [40, 41] made the observation that these RF experiments, which reflect the spectral function $A(\boldsymbol{k}, \omega)$, would observe a pairing gap $\Delta(T)$ which may be unrelated to superconducting order (except in the strict BCS regime). This was the beginning of a recognition that a pseudogap would be present, which is associated with stronger-than-BCS attractive interactions. Moreover, this pseudogap appears in the 'fermionic regime', that is when the fermionic chemical potential is positive [14].

A groundbreaking experimental paper [42] reported the first experimental implementation of this pairing gap spectroscopy in ^{6}Li over a range of fields corresponding to the BCS, BEC and unitary regimes. Accompanying this paper was a theoretical study [43] by Torma and co-workers based on the BCS–BEC crossover approach introduced earlier [40], but, importantly, generalized to include trap effects. This theoretical scheme, which was initially developed to address the high T_c cuprates [44], and also applied in [41], is the one that will be the focus of this paper. The calculations [43] showed reasonable agreement with experiment, and subsequent work [45] presented more quantitative comparisons of the spectra along with theoretically inferred estimates of the temperature, based on an adiabatic sweep thermometry [46]. Some of the first evidence that one was, indeed, observing a pairing gap (or pseudogap) in the normal phase was presented in [15], based on

this same thermometric approach and the data of the Innsbruck group [42].

In an important contribution, Yu and Baym pointed out [47] that the theoretical framework described above and summarized in equation (3) missed what have now become known as 'final state effects'. Moreover, this could be seen most clearly in sum rule constraints on the RF spectra. These final state effects can be understood as follows. Assume as the right panel of figure 1 that the condensed phase involves pairing among hyperfine channels 1 and 2 and that the excited atomic state is associated with hyperfine level 3. While the attractive interaction g_{12} drives the pairing, the excited atoms in 3 will also experience a residual interaction g_{13}, which may modify the RF spectra. In this way, these final state effects yield corrections to the lowest order current, shown in equation (3). Interestingly, the sum rule, now known as the 'clock shift' sum rule [48], shows that the first moment of the current sums to an internally consistent value, rather than a pre-determined constant. This will be discussed in section 4.1.

A new set of groundbreaking experiments from MIT have introduced a powerful way of exploiting and enhancing RF spectroscopy. With the implementation of tomographic techniques [49], the complication of studying the spectra in a trapped configuration can now be removed, so that a scan at different trap radii will yield an effectively homogeneous spectrum. Also important was the demonstration [31] that the entire collection of ^{6}Li superfluids with hyperfine levels 1 and 2 paired, as well as 1 and 3 as well as 2 and 3, are stable and can be probed in RF spectroscopy with variable RF transitions, $\Omega_{\rm L}$ (defined in the right panel of figure 1). In this way one has, in conjunction with a larger complex of superfluids, a way of tuning final state effects. Moreover, it was hoped that a proper choice of the superfluid and the RF transition can reduce the importance of these final state corrections and allow one to consider the simpler theory of equation (3).

The theoretical challenge of incorporating final state contributions has become very topical, in large part because of the existence of data in effectively 'homogeneous' systems through these tomographic techniques. In the absence of a trap one can more readily handle the higher order terms introduced by Yu and Baym [47]. With these corrections to equation (3) one may have a better opportunity to quantitatively fit the RF spectra. Very nice calculations [50, 51] of $I(\nu)$ in the homogeneous case consider the $T \approx 0$ superfluid and good agreement with experiment has been demonstrated [50]. Subsequent work [52] has addressed the entire range of temperatures where one can probe the RF contributions associated with pre-existing thermally excited quasi-particles. These are shown as a second branch of RF transitions in the right panel of figure 1. The body of work [45, 53] at general temperatures T makes the important point that the presence or absence of superfluid order (as long as $T < T^*$) will not lead to fundamentally different physics. This observation is in contrast to alternative calculations [50, 51, 54] which consider separately the $T \approx 0$ superfluid or the normal phase.

Along with these new developments has been an experimental and theoretical focus on population imbalanced gases [33, 55–59]. The observation [60] that extreme imbalance may drive the system to an exotic normal phase has captured the attention of the community. This exotic phase appears to be associated [61, 62] with the binding of a small number of reverse spins to the majority states and this signature is consistent with RF experiments, as shown theoretically [54, 63]. It should be stressed that this binding is not the same as pairing, which is a macroscopic many body phenomenon. But it may, nevertheless, smoothly evolve into pairing as one varies the concentration of reverse spins [64], and in this way diminishes the population imbalance.

With the growing appreciation for final state effects, an interesting controversy has recently emerged concerning slightly different data obtained on the 1-2 superfluid at unitarity. This involves the original Innsbruck experiment [42] and more recent data from the MIT group [31]. The latter series of studies have led the authors to inquire whether the pairing gap observations reported in [42] might instead be associated with final state effects. We comment on this possibility in section 6.3 of the paper, where we argue on behalf of the original interpretation in [42].

Finally, recent experiments on ^{40}K from the JILA group [27] have now demonstrated that it is possible to measure the spectral functions directly using momentum resolved RF pairing gap spectroscopy over a range of magnetic fields throughout the BCS–BEC crossover. These experiments are able to resolve the kinetic energy ϵ_k, and thereby the three-dimensional momentum distribution of the RF-excited (or 'out-coupled') state 3 atoms. Since the momentum of the RF photon is effectively negligible, the momenta of the out-coupled atoms can then be used to deduce that of the original 1-2 or paired states. There is a substantial advantage in using ^{40}K over the more widely studied ^{6}Li since, for the usual Feshbach resonance around 202 G, there are no nearby competing resonances to introduce complications from final state interactions [47, 50–52, 63]. This powerful tool, which we have seen has a strong analogy with ARPES spectra, opens the door for testing the fundamentals of the many body theory which underly this BCS–BEC crossover. As we show later in section 6.3, it may also help to remove ambiguity plaguing the interpretation [31, 42] of momentum integrated RF experiments by establishing a clear dispersion signature of pairing.

2.3. *Key features of ARPES data on cuprates*

We outlined earlier three issues around which much of the cuprate photoemission studies can be organized. These are characterizations and modeling of the fermionic self-energy, of the pseudogap phase and of the effects of coherence as the superconductor passes from above to below $T_{\rm c}$. Figure 2 is a plot showing the behavior of the excitation gap which addresses the first of these three issues. Plotted here is the pairing gap inferred from the leading edge in the photoemission experiments as a function of temperature. The temperature T^* can be read off as the temperature where the gap first appears. The three different curves correspond to three different doping concentrations which one can interpret in the framework of BCS–BEC crossover as corresponding to three different values

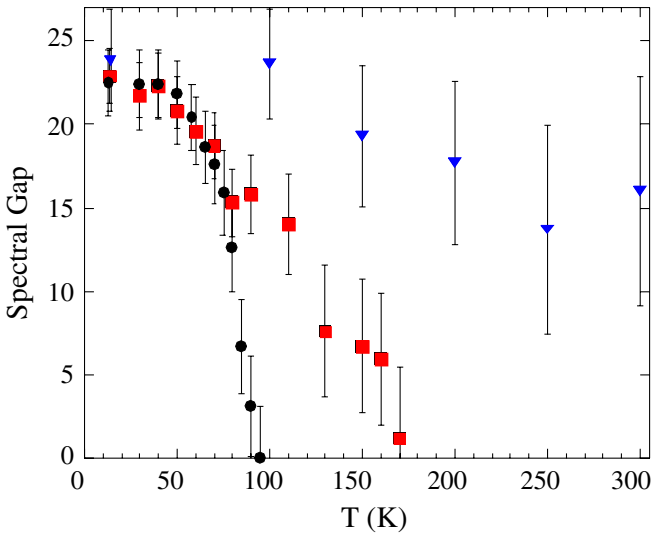

Figure 2. Temperature dependence of the excitation gap from the ARPES measurement for slightly overdoped (filled (black) circles, $T_c = 87$ K), underdoped ((red) squares, $T_c = 83$ K) and highly underdoped ((blue) inverted triangles, $T_c = 10$ K) single-crystal BSCCO samples (taken from [65]). There exists a pseudogap phase above T_c in the underdoped regime. (Color online.) Reprinted by permission from Macmillan Publishers Ltd: *Nature* (**382** 51–4), copyright (2006).

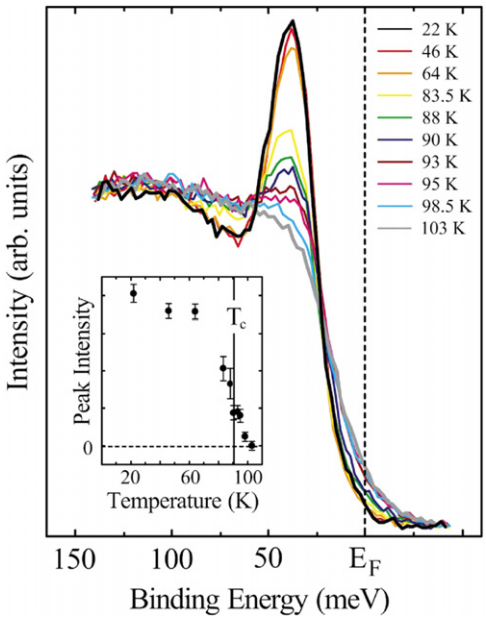

Figure 3. Temperature dependent photoemission spectra from optimally doped Bi2212 ($T_c = 91$ K), angle integrated over a narrow cut at $(\pi, 0)$. Inset: superconducting peak intensity versus temperature. After [28]. Note the sharpening of the peaks as temperature is lowered below T_c. (Color online.) Reprinted figure with permission from Damascelli R *et al* 2003 *Rev. Mod. Phys.* **75** 473. Copyright (2003) by the American Physical Society.

for the attraction strength, since they correspond to three different values for the pairing onset T^*.

Several key points can be made. The transition temperatures for phase coherent order are not evident when one studies the pairing gap, as shown in the figure except, perhaps, in the sample with the lowest T^* corresponding to the highest doping concentration. In this case $T^* \approx T_c$ as in the BCS limit. In general, in the presence of a pseudogap, the higher is T^* the lower is T_c, which is consistent with what one expects for BCS–BEC crossover on a lattice [66–69]. Because the behavior varies so smoothly from above to below T_c one says that the pseudogap smoothly evolves into the excitation gap of the superfluid phase (sometimes called the 'superconducting gap'). Indeed, independent experiments [29] show that these two have the same d-wave symmetry.

Ideally, one would like to obtain the analogous plots which show the temperature dependence of the pairing gap in the cold Fermi gases, using RF spectroscopy in the BCS, unitary and BEC regimes. It should be noted that none of the cuprate curves represent the BEC case. Even though the ratio T^*/T_c can be quite large due to lattice effects [66, 70, 71], the high temperature superconductors are all in the fermionic regime.

In figure 3 the cuprate photoemission spectra near optimal doping ($T_c \approx 91$ K) are plotted for a range of different temperatures in order to exhibit the effects of emerging phase coherence. This figure represents angle integrated spectra over a cut near the d-wave anti-node (where the gap is largest). What is most striking here is the fact that a sharp quasi-particle peak emerges only below T_c. Above T_c there is a pairing gap, but it is associated with a relatively poorly defined (gapped) quasi-particle. In the BCS–BEC crossover scenario, one might view this as representing short lived, but non-condensed pairs, which only below T_c can become long lived and stable.

Also of interest in the figure is a feature known as the dip–hump structure which is associated with superconducting coherence. There is still controversy over the origin of these effects, but some [30] have correlated them with specific bosonic modes which couple to the fermions and appear in the self-energy.

In a similar vein, it would be interesting to have more complete analogous studies using RF spectra on the cold gases as the system varies from above to below T_c. Just what the precise signatures of superfluid coherence are, and whether there is evidence that short lived non-condensed pair states become longer lived below T_c, needs to be addressed. Here one must (perhaps through tomography) overcome the complexity introduced because these gases are contained in a trap.

3. General theoretical background

3.1. BCS Leggett T-matrix theory

This paper will address the theory behind RF spectra and photoemission in the cuprates in the context of one particular approach to BCS–BEC crossover based on the BCS-Leggett ground state. Here, however, we generalize to finite temperatures T. There is an alternative approach [50] to crossover, based on the Nozieres–Schmitt-Rink scheme [70], which involves another ground state. Because of the flexibility of the BCS-Leggett scheme which can readily be generalized to include trap effects within the superfluid phase, as well as population imbalance, we choose this alternative. Another major advantage (from our perspective) is that it is not plagued by issues associated with a first order transition [72] at T_c.

These effects are related to analogous behavior [73] in mean field theories of the Bose gas. Interpretation of the cuprate data, which shows a smooth evolution through T_c, would be problematic in the presence of first order effects. A more detailed discussion of these two distinct approaches to BCS–BEC crossover is given in [23].

We briefly summarize the key equations which emerge from our T matrix scheme [14, 23]. Within the present approach there are two contributions to the full T-matrix:

$$t = t_{\rm pg} + t_{\rm sc}, \tag{5}$$

where

$$t_{\rm sc}(Q) = -\frac{\Delta_{\rm sc}^2}{T}\delta(Q), \tag{6}$$

and $\Delta_{\rm sc}$ is the superfluid (sc) order parameter. Similarly, we have two terms for the fermion self-energy:

$$\Sigma(K) = \Sigma_{\rm sc}(K) + \Sigma_{\rm pg}(K) = \sum_Q t(Q)G_0(Q-K). \tag{7}$$

Throughout this paper, we adopt a four-vector notation: $Q \equiv (\mathrm{i}\Omega_l, \boldsymbol{q})$, $K \equiv (\mathrm{i}\omega_n, \boldsymbol{k})$, and $\sum_Q \equiv T\sum_l \sum_{\boldsymbol{q}}$, $\sum_K \equiv T\sum_n \sum_{\boldsymbol{k}}$, where ω_n and Ω_l are the odd and even Matsubara frequencies, respectively. It then follows that

$$\Sigma_{\rm sc}(\boldsymbol{k}, \mathrm{i}\omega_n) = \frac{\Delta_{\rm sc}^2}{\mathrm{i}\omega_n + \epsilon_{\boldsymbol{k}} - \mu}. \tag{8}$$

Throughout, the label pg corresponds to the 'pseudogap' and the corresponding non-condensed pair propagator is given by

$$t_{\rm pg}(Q) = \frac{U}{1 + U\chi(Q)}, \tag{9}$$

where the pair susceptibility $\chi(Q)$ has to be properly chosen to arrive at the BCS-Leggett ground state equations and U is the attractive pairing interaction. We have also assumed a short range contact potential, which is appropriate for atomic Fermi gases. We impose the natural condition that below T_c there is a vanishing chemical potential for the non-condensed pairs

$$\mu_{\rm pair} = 0, \tag{10}$$

which means that $t_{\rm pg}(Q)$ diverges at $Q = 0$ when $T \leqslant T_c$. Thus, we approximate [74, 75] $\Sigma_{\rm pg}(K)$ to yield

$$\Sigma_{\rm pg}(K) \approx -G_0(-K)\Delta_{pg}^2 \qquad T \leqslant T_c, \tag{11}$$

with

$$\Delta_{\rm pg}^2 \equiv -\sum_{Q\neq 0} t_{\rm pg}(Q). \tag{12}$$

It follows that we have the usual BCS-like form for the self-energy:

$$\Sigma(\boldsymbol{k}, \mathrm{i}\omega_n) \approx \frac{\Delta^2}{\mathrm{i}\omega_n + \epsilon_{\boldsymbol{k}} - \mu}, \qquad (T \leqslant T_c) \tag{13}$$

with

$$\Delta^2(T) = \Delta_{\rm pg}^2(T) + \Delta_{\rm sc}^2(T). \tag{14}$$

As is consistent with the standard ground state constraints, $\Delta_{\rm pg}$ vanishes at $T \equiv 0$, where all pairs are condensed.

Using this self-energy, one determines G and thereby can evaluate $t_{\rm pg}$. Then the condition that the non-condensed pairs have a gapless excitation spectrum ($\mu_{\rm pair} = 0$) becomes the usual BCS gap equation, except that it is the excitation gap Δ and not the order parameter $\Delta_{\rm sc}$ which appears here. We then have from equation (10)

$$1 + U\sum_{\boldsymbol{k}} \frac{1 - 2f(E_{\boldsymbol{k}})}{2E_{\boldsymbol{k}}} = 0, \qquad T \leqslant T_c. \tag{15}$$

For consistency we take for the pair susceptibility

$$\chi(Q) = \sum_K G_0(Q-K)G(K). \tag{16}$$

Here $G = (G_0^{-1} - \Sigma)^{-1}$ and G_0 are the full and bare Green's functions, respectively.

Similarly, using

$$n = 2\sum_K G(K), \tag{17}$$

one derives

$$n = \sum_{\boldsymbol{k}} \left[1 - \frac{\epsilon_{\boldsymbol{k}} - \mu}{E_{\boldsymbol{k}}} + 2\frac{\epsilon_{\boldsymbol{k}} - \mu}{E_{\boldsymbol{k}}} f(E_{\boldsymbol{k}})\right], \tag{18}$$

which is the natural generalization of the BCS number equation. The final set of equations which must be solved is rather simple and given by equations (12), (15) and (18). Note that in the normal state (where $\mu_{\rm pair}$ is non-zero), equation (11) is no longer a good approximation, although a natural extension can be readily written down [53].

We stress that the approximation in equation (11) is not central to the physics, but it does greatly simplify the numerical analysis. One can see that correlations which do not involve pairing, such as Hartree terms, are not included here. This is what is required to arrive at the BCS-Leggett ground state. It should be clear that, in principle, the T-matrix approach discussed here is more general and that in order to address experiments at a more quantitative level it will be necessary to go beyond equation (11). These neglected effects can be seen to enter via 'G_0G_0' correlations in the pair susceptibility $\chi(Q)$ of the T-matrix. They also incorporate Hartree corrections which will ultimately have to be included for quantitative comparison with experiment. At high temperatures $T \approx T^*$, when pairing is weak they were studied some time ago [76], and at general temperatures in the normal phase, they were compared [74] with the more strongly pair-correlated 'GG_0' theory of this paper. Various groups [50, 54] have included these contributions, which are particularly important for highly imbalanced gases [54, 62, 63]. These weaker correlation terms are also seen to give rise to a pseudogap [16, 54, 74], albeit of somewhat different character than is found in the present BCS-Leggett formalism.

3.2. Generalization to include population imbalance

One major advantage of the BCS-Leggett approach is that it is straightforwardly generalized to include a population

imbalanced superfluid. We begin by summarizing the general equations associated with the so-called 'Sarma state', corresponding to a uniformly polarized BCS superfluid. This is to be distinguished from the phase separated state [55, 77].

The gap equation is now given by

$$0 = \frac{1}{U} + \sum_{k} \frac{1 - 2\bar{f}(E_k)}{2E_k}. \tag{19}$$

Here we define the average

$$\bar{f}(x) \equiv [f(x+h) + f(x-h)]/2, \tag{20}$$

where $f(x)$ is the Fermi distribution function. In addition we define $\mu = (\mu_\uparrow + \mu_\downarrow)/2$ and $h = (\mu_\uparrow - \mu_\downarrow)/2$, $E_k = \sqrt{\xi_k^2 + \Delta^2}$, $E_{k\uparrow} = -h + E_k$ and $E_{k\downarrow} = h + E_k$, where $\xi_k = \epsilon_k - \mu$.

There are now two number equations given by

$$n = 2\sum_{k} \left[v_k^2 + \frac{\xi_k}{E_k} \bar{f}(E_k) \right], \tag{21a}$$

$$\delta n = \sum_{k} [f(E_k - h) - f(E_k + h)], \tag{21b}$$

where $n = n_\uparrow + n_\downarrow$ is the total atomic density, $\delta n = n_\uparrow - n_\downarrow > 0$ is the number difference and $\delta \equiv \delta n/n$ is the polarization. Here the coefficients u_k^2, $v_k^2 = (1 \pm \xi_k/E_k)/2$ are formally the same for both the polarized and unpolarized systems.

Finally, one has to recompute $\Delta_{\rm pg}^2$, using the same equation as previously:

$$\Delta_{\rm pg}^2(T) = \Delta^2(T) - \Delta_{\rm sc}^2(T) = -\sum_{Q \neq 0} t_{\rm pg}(Q) \tag{22}$$

and presuming equation (9) except that the pair susceptibility appearing here satisfies

$$\chi(Q) = \tfrac{1}{2}[\chi_{\uparrow\downarrow}(Q) + \chi_{\downarrow\uparrow}(Q)]. \tag{23}$$

As before, we have the product of one dressed and one bare Green's function

$$\chi_{\uparrow\downarrow}(Q) = \sum_{K} G_{0\uparrow}(Q - K) G_\downarrow(K), \tag{24a}$$

$$\chi_{\downarrow\uparrow}(Q) = \sum_{K} G_{0\downarrow}(Q - K) G_\uparrow(K). \tag{24b}$$

Further details are presented in [53].

3.3. Linear response theory and RF

In the RF experiments [42], one focuses on three different atomic hyperfine states of the ^{6}Li atom. The two lowest states, $|1\rangle$ and $|2\rangle$, participate in the superfluid pairing. These correspond to $\uparrow$ and $\downarrow$. The higher state, $|3\rangle$, is effectively a free atom excitation level; it is unoccupied initially. An RF field, at sufficiently large frequency, will drive atoms from state $|2\rangle$ to $|3\rangle$.

We presume the usual grand canonical Hamiltonian $H - \mu N$ describes states $|1\rangle$ and $|2\rangle$. We have outlined in section 3.1 the procedure for handling pairing correlations in this 1-2 channel. The Hamiltonian characterizing state $|3\rangle$ is given by

$$H_3 - \mu_3 N_3 = \sum_{k} (\epsilon_k - \mu_3) c_{3,k}^\dagger c_{3,k},$$

where ϵ_k is the atomic kinetic energy, $c_{3,k}$ is the annihilation operator for state $|3\rangle$, and μ_3 is the chemical potential of $|3\rangle$. In addition, there is a transfer matrix element $T_{k,p}$ from $|2\rangle$ to $|3\rangle$ given by

$$H_T = \sum_{k,p} (T_{k,p}\, c_{3,p}^\dagger c_{2,k} + \text{h.c.}).$$

For plane wave states, $T_{k,p} = T_{23}\delta(\boldsymbol{q}_{\rm L} + \boldsymbol{k} - \boldsymbol{p})\delta(\omega_{kp} - \omega_{\rm L})$. Here $q_{\rm L} \approx 0$ and $\omega_{\rm L}$ are the momentum and energy of the RF field, and ω_{kp} is the energy difference between the initial and the final states. In what follows we will set the magnitude of the tunneling matrix element to unity, without loss of generality. It should be stressed that unlike conventional superconductor-normal tunneling, here one requires not only conservation of energy but also conservation of momentum.

The RF current is defined as

$$I = -\langle \dot{N}_2 \rangle = -\mathrm{i}\langle [H, N_2] \rangle.$$

Using standard linear response theory [39] one finds

$$I(\nu) = -\frac{1}{\pi} \mathrm{Im}[D^{\rm R}(\nu + \mu - \mu_3)].$$

Here we introduce the retarded response function $D^{\rm R}(\omega) \equiv D(\mathrm{i}\omega_n \to \omega + \mathrm{i}0^+)$.

At the lowest order of approximation the linear response kernel D can be expressed in terms of single particle Green's functions as

$$D_0(Q) = T \sum_{K} G_0^{(2)}(K) G^{(3)}(K + Q),$$

where $K = (\boldsymbol{k}, \omega_n)$ and $Q = (\boldsymbol{0}, \Omega_n)$. (We use the convention $\hbar = k_{\rm B} = 1$.) Green's function can then be expressed in terms of spectral functions. After Matsubara summation we obtain

$$I_0(\nu) = \frac{1}{4\pi^2} \int \mathrm{d}\epsilon \sum_{k} A(\boldsymbol{k}, \epsilon) A_3(\boldsymbol{k}, \bar{\epsilon}) [f(\bar{\epsilon}) - f(\epsilon)], \tag{25}$$

with $\bar{\epsilon} = \epsilon + \nu + \mu - \mu_3$, ν is the RF detuning.

We substitute in the known spectral function for state $|3\rangle$, $A_3(\boldsymbol{k}, \epsilon) = 2\pi\delta(\epsilon - \xi_{k,3})$, so that the RF response then depends on the spectral function associated with the superfluid component $|2\rangle$: $A(\boldsymbol{k}, \epsilon) \equiv -2\,\mathrm{Im}\, G(\boldsymbol{k}, \epsilon + \mathrm{i}0^+)$. Then the lowest order RF current can be written as

$$I_0(\nu) = -\frac{1}{2\pi} \sum_{k} A(\boldsymbol{k}, \xi_k - \nu) [f(\xi_k - \nu) - f(\xi_{k,3})]. \tag{26}$$

In practice, state 3 is unoccupied; thus the second Fermi function in brackets vanishes.

3.4. BCS-Leggett model for self energy

The current $I_0(\nu)$ at the leading order level depends on the fermionic spectral function, which, in turn, depends on the fermionic self-energy. In this section we discuss the nature of the self-energy which will enter into an analysis of both photoemission and RF spectroscopy.

To arrive at the BCS-Leggett ground state equations, we have seen that, after analytical continuation, the self-energy is given by $\Sigma(\boldsymbol{k}, \omega) = \Sigma_{\rm sc}(\boldsymbol{k}, \omega) + \Sigma_{\rm pg}(\boldsymbol{k}, \omega)$, where

$$\Sigma(\boldsymbol{k}, \omega) = \frac{\Delta_{\rm sc}^2}{\omega + \epsilon_{\boldsymbol{k}} - \mu} + \Sigma_{\rm pg}(\boldsymbol{k}, \omega) \tag{27}$$

$$\approx \frac{\Delta_{\rm sc}^2}{\omega + \epsilon_{\boldsymbol{k}} - \mu} + \frac{\Delta_{\rm pg}^2}{\omega + \epsilon_{\boldsymbol{k}} - \mu}, \qquad T \leqslant T_{\rm c}. \tag{28}$$

These equations follow, provided one makes the approximation contained in equation (11). In invoking this approximation we are in effect ignoring the difference between condensed and non-condensed pairs which cannot be strictly correct. The simplest correction to $\Sigma_{\rm pg}$ (which should apply above and below $T_{\rm c}$) is to write an improved form:

$$\Sigma_{\rm pg}(\boldsymbol{k}, \omega) \approx \frac{\Delta_{\rm pg}^2}{\omega + \epsilon_{\boldsymbol{k}} - \mu + {\rm i}\gamma} + \Sigma_0(\boldsymbol{k}, \omega). \tag{29}$$

Here the broadening $\gamma \neq 0$ and 'incoherent' background contribution Σ_0 reflect the fact that non-condensed pairs do not lead to *true* off-diagonal long-range order. While we can think of γ as a phenomenological parameter in the spirit of the high $T_{\rm c}$ literature [78, 79], there is a microscopic basis for considering this broadened BCS form [74, 80]. The precise value of γ and its T-dependence are not particularly important for the present purposes, as long as it is non-zero at finite T. For simplicity we generally take γ as a temperature independent constant. By contrast, $\Sigma_{\rm sc}$ is associated with long-lived condensed Cooper pairs, and is similar to $\Sigma_{\rm pg}$ but without the broadening.

It is important to stress that this same self-energy model has been applied to describe the spectral function in the pseudogap [44, 78, 79] and the superfluid phases [81] of the high temperature superconductors, where $\Sigma_0(\boldsymbol{k}, \omega) \equiv -{\rm i}\Gamma_0 \approx -{\rm i}\gamma$, is taken to be an imaginary constant. In the cuprate literature (presuming that equation (29) is appropriate to the normal and superfluid phase), it has been argued that the onset of coherence coincides with a dramatic decrease in γ below $T_{\rm c}$. Our own perspective is that equation (27) in conjunction with equation (29) is the more appropriate starting point. That is, there are two contributions to the self-energy below $T_{\rm c}$ and only one above. Thus one should not argue that γ precisely vanishes at $T_{\rm c}$ but rather there is a continuous conversion from non-condensed to condensed pairs as T is lowered within the superfluid phase. The non-condensed pairs below $T_{\rm c}$ have finite lifetime while the condensed pairs do not.

The resulting spectral function, based on equations (29) and (27), is given by

$$A(\boldsymbol{k}, \epsilon) = \frac{2\Delta_{\rm pg}^2 \gamma (\epsilon + \xi_{\boldsymbol{k}})^2}{(\epsilon + \xi_{\boldsymbol{k}})^2 (\epsilon^2 - E_{\boldsymbol{k}}^2)^2 + \gamma^2 (\epsilon^2 - \xi_{\boldsymbol{k}}^2 - \Delta_{\rm sc}^2)^2}. \tag{30}$$

Here, for convenience we do not show the effects of the Σ_0 term. Above $T_{\rm c}$, equation (30) is used with $\Delta_{\rm sc} = 0$. It can be seen that at all $\boldsymbol{k}$ and below $T_{\rm c}$, this spectral function contains a zero at $\epsilon = -\xi_{\boldsymbol{k}}$, whereas it has no zero above $T_{\rm c}$. This means that a clear signature of phase coherence is present, as long as $\gamma \neq 0$. In discussing the d-wave pairing of the cuprates we need to incorporate specific $\boldsymbol{k}$ dependent factors so that the gap parameters in the self-energy acquire the form $\Delta_{\boldsymbol{k},\rm sc} = \Delta_{\rm sc}\varphi_{\boldsymbol{k}}$ and $\Delta_{\boldsymbol{k},\rm pg} = \Delta_{\rm pg}\varphi_{\boldsymbol{k}}$, where we introduce $\varphi_{\boldsymbol{k}} = \cos(2\phi)$, to reflect the d-wave $\boldsymbol{k}$ dependence along the Fermi surface. We adopt a tight binding model for the band dispersion $\epsilon_{\boldsymbol{k}}$, $\epsilon_{\boldsymbol{k}} = 2t(2 - \cos k_x - \cos k_y) + 2t_z(1 - \cos k_z) - \mu$. It should be stressed that all gap parameters have the same $\boldsymbol{k}$ dependence so that the effects of anisotropy, which we will see later, are not present in the initial gap parameters but rather appear in the measured spectral gaps.

Finally, this analysis may be readily generalized to include the effects of population imbalance. We have for the spectral function of the minority

$$A_2(\boldsymbol{k}, \epsilon) = \frac{2\Delta_{\rm pg}^2 \gamma (\epsilon' + \xi_{\boldsymbol{k}})^2}{(\epsilon' + \xi_{\boldsymbol{k}})^2 (\epsilon'^2 - E_{\boldsymbol{k}}^2)^2 + \gamma^2 (\epsilon'^2 - \xi_{\boldsymbol{k}}^2 - \Delta_{\rm sc}^2)^2} \tag{31}$$

with $\epsilon' = \epsilon - h$.

Similarly, the spectral function for the majority is

$$A_1(\boldsymbol{k}, \epsilon) = \frac{2\Delta_{\rm pg}^2 \gamma (\epsilon'' + \xi_{\boldsymbol{k}})^2}{(\epsilon'' + \xi_{\boldsymbol{k}})^2 (\epsilon''^2 - E_{\boldsymbol{k}}^2)^2 + \gamma^2 (\epsilon''^2 - \xi_{\boldsymbol{k}}^2 - \Delta_{\rm sc}^2)^2} \tag{32}$$

with $\epsilon'' = \epsilon + h$.

There are instances where it is problematic to include the effects associated with the finite lifetime γ. This occurs when we compute the effects of final state interactions. At this strict 'mean field' (mf) level we drop the factor γ, thereby losing the distinction between condensed and non-condensed pairs. In this case the spectral function (which we display here for the polarized gas case) is associated with majority (1) and minority (2) contributions:

$$A_1^{\rm mf}(\boldsymbol{k}, \epsilon) = 2\pi[u_{\boldsymbol{k}}^2 \delta(\epsilon - E_{\boldsymbol{k},\uparrow}) + v_{\boldsymbol{k}}^2 \delta(\epsilon + E_{\boldsymbol{k},\downarrow})],$$

$$A_2^{\rm mf}(\boldsymbol{k}, \epsilon) = 2\pi[u_{\boldsymbol{k}}^2 \delta(\epsilon - E_{\boldsymbol{k},\downarrow}) + v_{\boldsymbol{k}}^2 \delta(\epsilon + E_{\boldsymbol{k},\uparrow})],$$

with $E_{\boldsymbol{k},\uparrow} = E_{\boldsymbol{k}} - h$ and $E_{\boldsymbol{k},\downarrow} = E_{\boldsymbol{k}} + h$. We stress again, however, that here Δ contains non-condensed pair effects through equation (14).

3.5. Analytical results for the leading order RF current

It is possible to obtain analytical results for the leading order current at general temperatures T in this strict mean field theory. Here one integrates over the momentum to find

$$I_0(\nu) = \frac{1}{8\pi^2}\frac{\Delta^2}{\nu^2}[1 - f(E_0)]k_0, \qquad (\nu > \nu_1), \tag{33}$$

$$I_0(\nu) = \frac{1}{8\pi^2}\frac{\Delta^2}{\nu^2} f(E_0)k_0, \qquad (\nu_2 < \nu < 0) \tag{34}$$

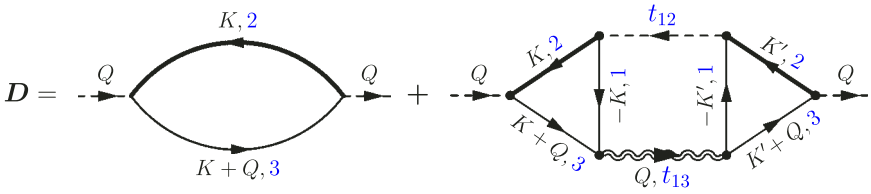

Figure 4. Feynman diagrams for the RF response function $D(Q)$. The left bubble is the lowest order D_0, whereas the right diagram, $D_{\rm AL}$, is associated with final state effects. Here thin (thick) lines stand for bare (full) fermion propagators, the dashed line for t_{12}, approximated as the condensate, and double wiggly line for t_{13}. The numbers (blue) indicate the hyperfine levels. Here $Q = (\mathrm{i}\Omega_n, \mathbf{0})$ for the RF field.

with

$$E_0 = \left|\frac{\nu^2 + \Delta^2}{2\nu}\right|, \qquad k_0^2 = \mu + \frac{\nu^2 - \Delta^2}{2\nu}.$$

The frequency regimes associated with the negative and positive continua are given by $-(\sqrt{\mu^2+\Delta^2}+\mu) \leqslant \nu \leqslant 0$ and $\nu \geqslant \sqrt{\mu^2+\Delta^2} - \mu$. In the above equations $\nu_2 \equiv -(\sqrt{\mu^2+\Delta^2}+\mu)$ and $\nu_1 \equiv \sqrt{\mu^2+\Delta^2}-\mu$. It can be seen that there are contributions for both negative and positive detuning. At strictly zero temperature, the Fermi function vanishes, and we have only the positive continuum:

$$I_0(\nu) = \frac{1}{8\pi^2}\frac{\Delta^2}{\nu^2}\sqrt{\mu + \frac{\nu^2 - \Delta^2}{2\nu}}. \tag{35}$$

In the same way, it is also possible to write down a closed form expression for the polarized case at general T as well. Because the expressions are more cumbersome, we defer this to appendix A.

3.6. Behavior in traps in absence of final state effects

Once the trap is incorporated, one has to solve for the current at each position r and then integrate in the form

$$I_\sigma(\nu) = \int \mathrm{d}^3 r\, I(r,\nu) n_\sigma(r), \tag{36}$$

where $n_\sigma(r)$ represents the particle density within the trap and $\sigma = 1, 2$ are the different hyperfine levels of the superfluid. To handle the trap effects we assume a spherically symmetrical harmonic oscillator potential $V(r) = m\bar{\omega}^2 r^2/2$. The density, excitation gap and chemical potential which vary along the radius can be determined [53] using the local density approximation (LDA).

It should be stressed that the density and gap profiles ($n_\sigma(r)$ and $\Delta(r)$) in general involve pseudogap or non-condensed pair effects. The strict mean field theory, which often gives a reasonable approximation to the spectral functions, is not adequate for obtaining these trap profiles. Thus, even when analyzing tomographic RF data, one has to include the full effects of these pair excitations [53], effectively through $\Delta_{\rm pg}^2(r)$ and non-zero $\mu_{\rm pair}(r)$.

4. Final state effects in homogeneous unpolarized system

We now turn [52] to the inclusion of final state effects which go beyond the leading order diagram. It is complicated to handle these contributions for the inhomogeneous case. Thus we focus here on computing the RF current in the homogeneous limit. We formulate the finite T, RF problem using a diagrammatic scheme, where the diagrams for the RF response function, $D(Q)$, are shown in figure 4. The leading order term D_0 appears as the first term on the right hand side and the second contribution is associated with the Aslamazov–Larkin (AL) diagram (called $D_{\rm AL}$). The full RF current, given by the retarded response function, is $I(\nu) \equiv -(1/\pi)\,\mathrm{Im}\, D^{\rm R}(\Omega)$, where $\Omega \equiv \nu + \mu - \mu_3$.

The approximation compatible with equation (11) is effectively equivalent to treating the $D_{\rm AL}$ in figure 4 at the BCS mean field level, leading to the opposite momenta $\pm K$ for particles 1 and 2 in the diagram. $D_{\rm AL}(Q)$ depends on Δ, not $\Delta_{\rm sc}$, and incorporates final state effects via the interactions g_{12} between 1 and 2 and g_{13} between 1 and 3. We neglect the effects arising from the interaction between 2 and 3. This is consistent with the approach in [48]. This second term has appeared previously in studies on superfluid density [82]. Our formulation of the finite T, RF problem can be made compatible with the diagrams in [50], although attention in that paper was restricted to very low temperatures. Our diagrammatic scheme reduces at $T = 0$ to the approach of [51].

In order to evaluate the AL term, we begin by writing out the relevant T-matrices

$$t_{12}^{-1}(Q) = g_{12}^{-1} + \sum_K G_1(K) G_2^0(Q-K), \tag{37}$$

$$t_{13}^{-1}(Q) = g_{13}^{-1} + \sum_K G_1(K) G_3^0(Q-K), \tag{38}$$

where g_{12} and g_{13} parametrize the interaction between 1 and 2, and 1 and 3, respectively. We can also introduce the s-wave scattering lengths, a_{13} (and a_{12}) in the 1-3 (and 1-2) channels, respectively.

Thus

$$t_{13}^{-1}(Q) = \frac{m}{4\pi a_{13}} + \chi_{13}(Q), \tag{39}$$

where

$$\chi_{13}(Q) = -\sum_k \left[\frac{1 - f(E_k) - f(\xi_{k,3})}{\mathrm{i}\Omega_n - E_k - \xi_{k,3}} u_k^2 + \frac{f(E_k) - f(\xi_{k,3})}{\mathrm{i}\Omega_n + E_k - \xi_{k,3}} v_k^2 + \frac{1}{2\epsilon_k}\right]. \tag{40}$$

The AL diagram yields

$$D_{\rm AL}(Q) = \left[\sum_K F(K) G_3^0(K+Q)\right]^2 t_{13}(Q), \tag{41}$$

where

$$F(K) \equiv -\Delta G^{(2)}(K) G_0^{(1)}(-K) = \frac{\Delta}{(\mathrm{i}\omega_l)^2 - E_k^2}. \quad (42)$$

This contribution can be rewritten as

$$D_{\mathrm{AL}}(Q) \equiv D_2^2(Q) t_{13}(Q), \quad (43)$$

where we have defined

$$D_2(Q) \equiv \sum_K F(K) G_3^0(K+Q) = \sum_K \frac{\Delta}{2E_k} \left[\frac{1 - f(E_k) - f(\xi_{k,3})}{\mathrm{i}\Omega_n - E_k - \xi_{k,3}} - \frac{f(E_k) - f(\xi_{k,3})}{\mathrm{i}\Omega_n + E_k - \xi_{k,3}} \right]. \quad (44)$$

Then the full set of diagrams shown in figure 4 can be combined to yield

$$D(Q) = D_0(Q) + \frac{[D_2(Q)]^2}{m/4\pi a_{13} + \chi_{1,3}(Q)}. \quad (45)$$

After analytical continuation and change of variables, we have $\Omega \pm E_k - \xi_{k,3} = \nu \pm E_k - \xi_k$. Importantly, the denominators here are the same as those which appear in t_{12}. Furthermore, at $\nu = 0$, $f(\xi_{k,3})$ is canceled out so that

$$t_{13}^{-1}(0) = (g_{13}^{-1} - g_{12}^{-1}) + t_{12}^{-1}(0) = g_{13}^{-1} - g_{12}^{-1}. \quad (46)$$

It follows that the complex functions $D_0(Q)$, $\chi_{1,3}(Q)$ and $D_2(Q)$ are the same as their wave function calculation counterparts [51] when the pairing gap Δ is chosen to be order parameter Δ_{sc} and $T = 0$. It is ν, not Ω, that should be identified with the experimental RF detuning.

After some straightforward algebra (with details in appendix B), we find for the RF current

$$I(\nu) = \left[\frac{1}{g_{12}} - \frac{1}{g_{13}} \right]^2 \frac{I_0(\nu)}{|t_{13}^{-1,R}(\nu)|^2} = -\frac{1}{\pi} \left(\frac{m}{4\pi a_{13}} - \frac{m}{4\pi a_{12}} \right)^2 \frac{\mathrm{Im} D_0^R(\nu)}{|t_{13}^{-1,R}(\nu)|^2} = -\frac{1}{\pi} \left[\frac{m}{4\pi a_{13}} - \frac{m}{4\pi a_{12}} \right]^2 \frac{\Delta^2}{\nu^2} \mathrm{Im}\, t_{13}^R(\nu). \quad (47)$$

Moreover, in the special case, when $a_{13} = a_{12}$ then $I(\nu) = (n_2 - n_3)\delta(\nu)$, as shown in appendix C.

Equations (47) are the central result. It should be clear that final state effects in the RF current directly reflect the T-matrix in the 1-3 channel. In general, features in the RF spectra derive from the poles and the imaginary parts of $D_0(Q)$, $\chi_{1,3}(Q)$ and $D_2(Q)$.

The spectrum may contain a bound state associated with poles at ν_0 in t_{13}, as determined by $t_{13}^{-1}(\nu_0) = 0$. This leads to the so-called 'bound–bound' transition. In addition, there is a continuum associated with both the numerator and the denominator in the first of equations (47), with each contribution spanned by the limits of $\nu = \xi_k \pm E_k$, i.e. $-(\sqrt{\mu^2 + \Delta^2} + \mu) \leqslant \nu \leqslant 0$ and $\nu \geqslant \sqrt{\mu^2 + \Delta^2} - \mu$. The continuum at positive frequencies is primarily associated with breaking a pair and promoting the state 2 to state 3. This represents the so-called 'bound-free' transition. On the negative detuning side, the continuum is primarily associated with promoting to state 3 an already existing thermally excited 2 particle. The spectral weight of the negative continuum vanishes exponentially at low T.

4.1. Sum rules

Of importance in assessing any theoretical framework for computing the RF current are the two sum rules associated with the total integrated current and the first moment or 'clock shift' [48]. Using the Kramers–Kronig relations between $\mathrm{Re}\, t_{13}^{\mathrm{R}}$ and $\mathrm{Im}\, t_{13}^{\mathrm{R}}$, we prove in appendix D that, not only in the ground state but also at finite temperature, equation (47) satisfies

$$\int \mathrm{d}\nu\, I(\nu) = n_2 - n_3, \quad (48)$$

$$\int \mathrm{d}\nu\, \nu\, I(\nu) = \Delta^2 \frac{m}{4\pi} \left(\frac{1}{a_{12}} - \frac{1}{a_{13}} \right), \quad (49)$$

where n_2 and $n_3 (= 0)$ are the density of state 2 and 3 atoms, respectively. In this way we find for the clock shift a result which we write (for general polarizations, associated with the subscript σ) in the form

$$\bar{\nu}_\sigma = \frac{\int \mathrm{d}\nu\, \nu I_\sigma(\nu)}{\int \mathrm{d}\nu\, I_\sigma(\nu)} = \frac{\Delta^2}{n_\sigma - n_3} \frac{m}{4\pi} \left(\frac{1}{a_{12}} - \frac{1}{a_{13}} \right). \quad (50)$$

In the unpolarized case, this agrees with [48]. This sum rule is satisfied only when $a_{13} \neq 0$ and when both diagrammatic contributions are included. It is easy to show that at large ν, $I_0(\nu) \sim \nu^{-3/2}$, $\mathrm{Im}\, t_{13}^R \sim \nu^{-1/2}$, so that $I(\nu) \sim \nu^{-5/2}$, in agreement with [50]. Clearly, the first moment of $I(\nu)$ is integrable, whereas the first moment of $I_0(\nu)$ is not. Finally, equation (47) reveals that the spectral weight (including possible bound states) away from $\nu = 0$ will disappear when the gap Δ vanishes.

5. Physical picture and implications

In this section we lay the groundwork for a comparison between theory and experiment, which is presented in the following section. We address the various phase diagrams for the population balanced Fermi gases, including the (d-wave) lattice case, as well as for the imbalanced systems. We analyze a pedagogically useful set of figures which lay out the general behavior of the RF spectra with and without final state effects and with and without a trap. Importantly, we compare photoemission-based plots for the same parameter set as RF-based plots and address the key signatures of emerging superfluid coherence as one goes from above to below T_c.

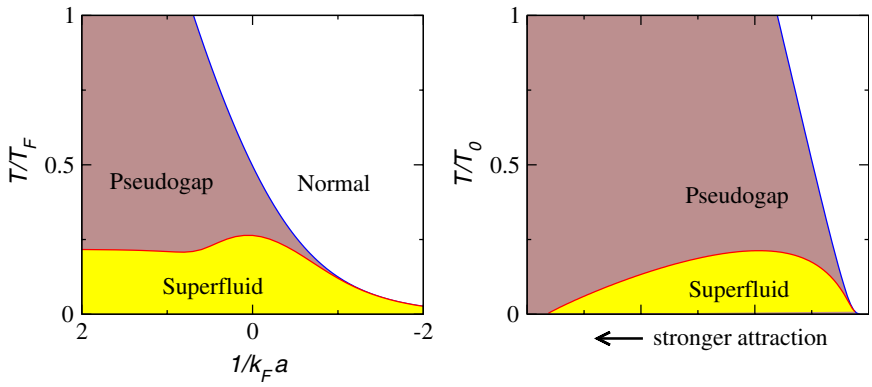

Figure 5. Phase diagram showing T_c and T^* for homogeneous s-wave Fermi gas superfluid (left) and for d-wave superfluid on a quasi-two-dimensional lattice; from [71]. Note that the BEC asymptote is finite in a Fermi gas and zero in the lattice case. Because the lattice phase diagram shows similarity to that of the cuprates, in future experiments it will be important to study the d-wave generalization of the attractive Hubbard model on an optical lattice.

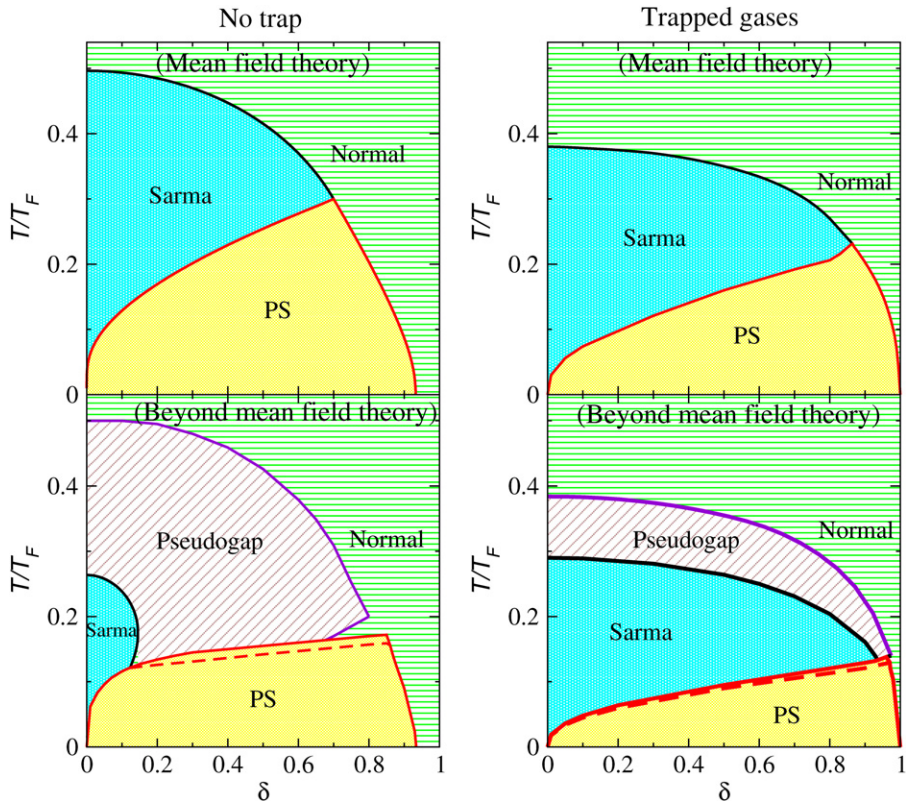

Figure 6. This summarizes the phase diagrams for polarized gases with and without a trap and with and without pairing fluctuations. The figure is based on [53, 58]. The figures on the left are for the homogeneous case and on the right for the trapped case. The mean field figures at the top show the reported tri-critical point. However, fluctuations (in the lower two plots) depress the superfluid phases. Here T_F is the Fermi temperature of an unpolarized non-interacting Fermi gas with the same total particle density.

5.1. Phase diagrams

The relevant phase diagrams to be used and referred to in our RF calculations have been obtained elsewhere. Shown in figure 5 are the curves for T_c and T^* comparing the phase diagram for an s-wave paired Fermi gas (left) and for a d-wave paired fermion system (right) on a quasi-two-dimensional lattice. The s-wave gas case is closely analogous to the results obtained using the approach of [70, 83]. The d-wave case was discussed earlier in [66] and more recently in the context of optical lattice calculations in [67, 71]. The seminal Nozieres–Schmitt-Rink paper pointed out a key fact which identifies a notable difference between the lattice and gas cases: the BEC limit has an asymptote of $T_c \to 0$ in the case of a lattice, whereas it is finite in a gas. Thus there is a relatively larger separation between T^* and T_c when fermions are present on a lattice as shown in the figure. We note that the d-wave case has a number of features in common [66, 67, 71] with the counterpart phase diagram [18] in the cuprates.

The phase diagrams for polarized (s-wave) Fermi gases are shown in figure 6. The four panels correspond to the effects

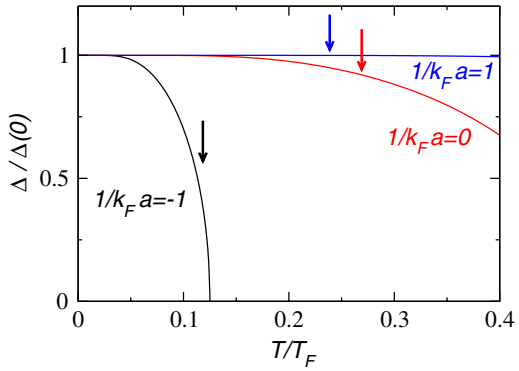

Figure 7. This figure shows the behavior of the excitation gap as a function of temperature[3] for the Fermi gases at three different scattering lengths. This should be compared with figure 2 for the cuprates. Arrows indicate locations of T_c.

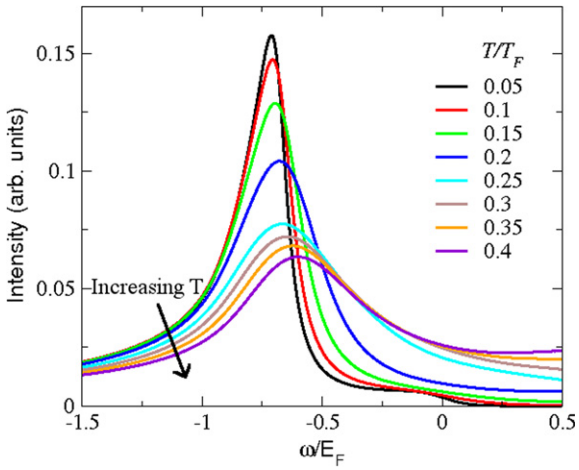

Figure 8. This is a photoemission-like plot for a homogeneous unitary Fermi gas based on equations (29) and (2). Here $T_c = 0.27T_F$ and $T^* \approx 0.5T_F$. The figure shows that the onset of superfluid coherence leads to a sharpening of the peak structure. We take γ to be $\Delta/2$. This figure can be compared with figure 2.

of including (or not) a trap and to the effects of including (or not) pairing fluctuations beyond strict mean field theory, which enter in the theory through the parameter Δ_{pg}^2. When we discuss the RF behavior of polarized gases we will use the full beyond-mean-field theory phase diagrams, although some of the calculations of the spectral function are performed at the strict mean field level.

Beyond the normal phase, there are three phases which appear [53, 58]: the Sarma phase, a phase separated (PS) state and a pseudogapped normal state, as indicated. We note that the treatment of the normal component of the phase separated state does not include correlations beyond those accounted for by Δ. As a result, these calculations overestimate the range of stability of phase separation. This issue has been nicely discussed in the theoretical literature [61, 62] with implications for RF spectra as well [54, 63]. The Sarma phase should be considered as the more correctly treated here and one notes an important finding: in the absence of a trap the regime of stability of the Sarma state is greatly reduced. This more restricted stability (seen by comparing the two lower figures) is associated with the fact that the excess majority fermions can be accommodated more readily in different spatial regions in a trap. The maximum polarization of this homogeneous Sarma phase is around $\delta = 0.2$ which is close to that reported experimentally [84].

5.2. *Comparison with the cuprates*

We present in figure 7 a plot of the excitation gap in the cold gases for three different values of the s-wave scattering length in units of $1/k_F a$ which are near unitarity ($a = \infty$) and on both the BCS and BEC sides. This figure should be compared with figure 2 for the cuprates. Here the excitation gap is estimated using equation (15) for all temperatures[3]. Also indicated on the curves is the value of the transition temperature. This figure makes it clear that pseudogap effects, which are essentially absent on the BCS side of resonance, are very apparent at unitarity, where the Fermi gas has a positive chemical potential.

[3] Above T_c one should ultimately include the effects associated with non-zero μ_{pair}. We ignore them here for simplicity and use strict mean field theory to estimate the excitation gap everywhere.

In both the unitary and BEC cases, Δ is roughly temperature independent below T_c.

Figure 8 represents a photoemission-like study, but for the parameters associated with a unitary (homogeneous) Fermi gas. Here the vertical axis plots the $\boldsymbol{k}$ integral of $I^{\text{photo}}(\boldsymbol{k}, \omega)$ based on equation (2) assuming a structureless matrix element M_0. This figure should be compared with the cuprate data in figure 3. The various curves correspond to different temperatures as indicated with $T_c = 0.25T_F$ and $T^* \approx 0.5T_F$. The self-energy is based on equation (29) for the non-condensed pair component with $\gamma = 0.25E_F$ and $\Sigma_0 = \Gamma_0 = 0.1E_F$. What is most notable about this figure is the progressive sharpening of the 'photoemission' peaks associated with the growth of coherence as T decreases. This same effect is seen in the cuprate data (figure 3). One notes here, however, that there is some shift of this peak position reflecting an increase in Δ with decreasing T, which is not seen in the cuprate data. This effect can be attributed to the fact that there is a substantially larger separation [67, 69, 71] between T^* and T_c in the case of a lattice (away from the BCS regime) than for a gas such as shown here. This is apparent in figure 5. Thus, there is more temperature dependence found in the excitation gap of the superfluid phase (if one compares with the same value of T^*).

5.3. *Overview of RF spectra: homogeneous case*

The top panel of figure 9 represents a plot of characteristic RF spectra for a unitary gas without final state effects and at a moderate temperature below T_c. Here we use strict mean field theory. Indicated in the figure are the various energy scales showing the location of the pairing gap Δ as well as the thresholds associated with the negative and positive continua. Spanned by $-(\sqrt{\mu^2 + \Delta^2} + \mu) \leqslant \nu \leqslant 0$ and $\nu \geqslant \sqrt{\mu^2 + \Delta^2} - \mu$, these are indicated as ν_2 and ν_1. These RF spectra exhibit a two peak structure, even in this homogeneous situation, with the lower peak corresponding

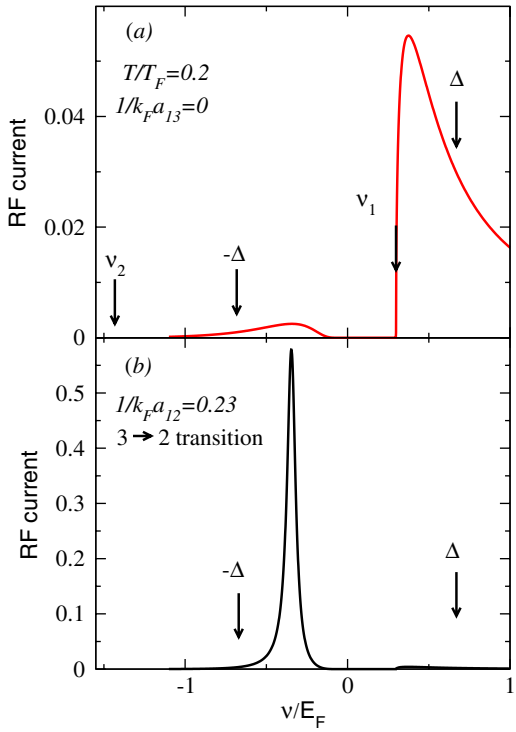

Figure 9. Pedagogical figure showing typical RF spectra of unitary homogeneous gas at a temperature somewhat below T_c. The various characteristic energy scales are labeled. Upper panel corresponds to absence of final state effects while lower panel includes final state effects in rather extreme limit of a (weakly) bound state in the negative continuum. This is the optimal situation for using the sum rules to extract Δ.

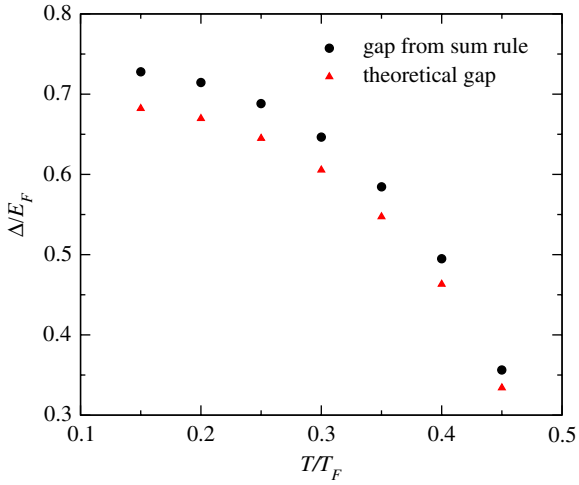

Figure 10. Based on previous figure and equation (50), plotted here are pairing gaps $\Delta(T)/E_F$ versus temperature as computed exactly and as computed from a limited integration, using the sum rule.

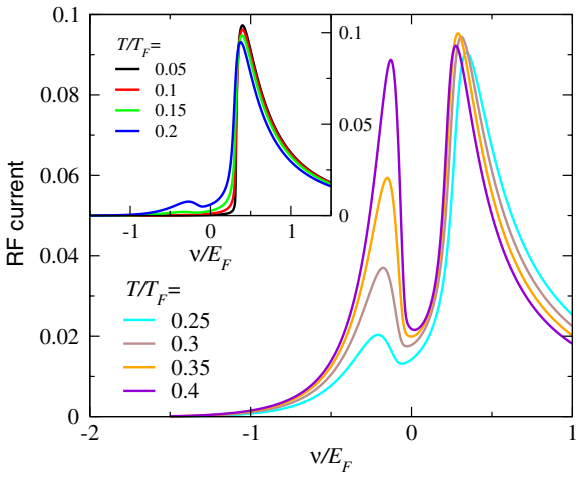

Figure 11. This is the RF counterpart of figure 8 for homogeneous unitary gas. The main body of the figure plots the higher T behavior and the inset shows the results at lower T when superfluid coherence is well established. Just as in photoemission, there appears to be a signature of this coherence in the RF spectra which is associated with a rather sharp threshold behavior, as seen in the inset.

to the negative continuum. This behavior was found earlier in [41], although subsequent normal state work [54] using the alternative (G_0G_0), more weakly correlated pair susceptibility, argued that only one peak would appear in a homogeneous system.

One can see from figure 9 that there is a substantial separation between the pairing gap value and the threshold ν_1 and there is very little in the figure to suggest a way of extracting the pairing gap. This has presented a dilemma for the field. One way to address this issue is to exploit the sum rule in equation (50) which is appropriate provided one includes final state effects. In the lower panel we show the same spectra when final state effects are included. We have chosen a very special case for illustrative purposes in which a (meta-stable) bound state overlaps the negative continuum [52]. This represents the most ideal example for exploiting sum rule constraints to extract the pairing gap. One can see here that because the bound state is in the negative continuum, the bulk of the spectral weight is confined to a narrow frequency weight spanning from ν_2 to 0.

In figure 10 we show the estimated values for the pairing gap Δ of a unitary gas obtained from the sum rule as integrated from $\nu = -2E_F$ to $\nu = +2E_F$ compared with the exact pairing gap. The accuracy is within 10%. To arrive at a case where the final state is on the BEC side of resonance is reasonably straightforward and the 1-3 superfluid, which exhibits this behavior, is now well studied by the MIT group [31]. However, we point out that for this unitary 1-3 superfluid and for typical values of k_F the bound state is deep and well removed from the continuum. By contrast, the case shown here results from a situation in which k_F is increased from the currently quoted experimental values by about a factor of 10. While this may not be easy to achieve in the near future, it does point to the advantage of exploiting final state effects to focus the spectral weight in the more well-confined, negative ν regime. Moreover, for a 1-3 superfluid on the BCS side of resonance, the pairing gap as obtained via sum rules is more accessible experimentally, as was pointed out [52] earlier.

We plot in figure 11 the homogeneous spectra in the absence of final state effects but now for the case in which we go beyond strict mean field theory and, thereby, differentiate the condensed and non-condensed pairs on the basis of equation (29). We have chosen the same parameters as in figure 8. In contrast to this earlier photoemission-

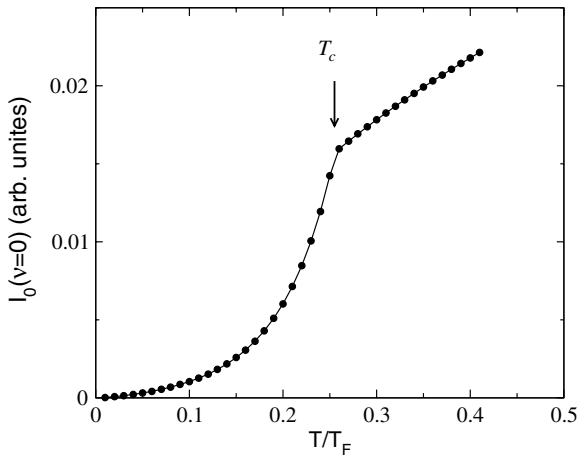

Figure 12. Evidence that T_c may show up as a feature in RF spectroscopy. Based on the results of figure 11, plotted here is the RF current magnitude at zero detuning (for a homogeneous balanced unitary gas without final state effects) as a function of temperature.

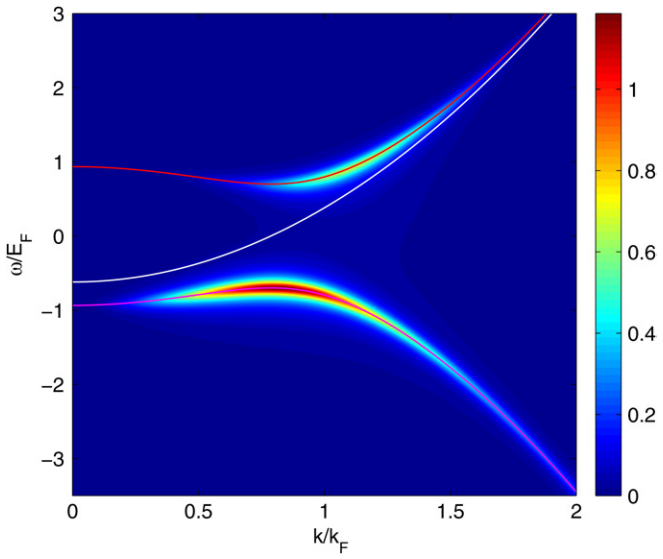

Figure 13. Contour plots of occupied spectral intensity for the homogeneous case at unitarity at $T/T_c \approx 1.9$. The top and bottom lines in the contour plots correspond to the two quasi-particle dispersions $\mu \pm \sqrt{((k^2/2m-\mu)^2+\Delta^2)}$ and the middle line is that of the free atom dispersion.

based calculation, one applies equation (3) to describe the RF experiments. Each of the curves corresponds to the same temperatures as their counterparts in figure 8. It can be seen that the shape of the RF spectra is very different from that of photoemission (even in the absence of final state effects), because of the constraint introduced by $\omega = \xi_k - \nu$ which appears in equation (3). There are two peak structures at higher T, even in this homogeneous situation, with the lower peak corresponding to the negative continuum.

The temperature regime is separated into the superfluid phase in the inset and the normal phase in the main body. The differences between the two sets of curves support the fact that there are signatures of superfluid coherence in RF spectroscopy. While there are no abrupt changes at T_c, nevertheless, like the quasi-particle peak sharpening seen in the cuprates (in figure 3) one sees some sharpening of the positive ν threshold as the temperature crosses T_c.

To quantify this, figure 12 shows a plot of the zero detuning current for this balanced gas as a function of temperature. There is a feature at T_c which may make it possible, in principle, to extract this transition temperature from high resolution RF experiments. Thus, there are indications in the RF spectrum of superfluid coherence, as seen in photoemission plots. RF techniques may ultimately prove useful for making quick estimates of whether these atomic systems are in the superfluid phase or not without resorting to the much more complex experiments which involve vortex generation. Moreover one infers from this figure that the negative continuum begins to be perceptible as the temperature approaches T_c.

5.4. Momentum resolved RF

We now turn to momentum resolved RF spectra which effectively measure the occupied spectral intensity. Later in figure 21, we will study some potentially analogous experiments which address momentum resolved (or 'angle resolved') photoemission in the cuprates. In figure 13, we present a contour map of the occupied spectral intensity as a function of single particle energy and wave vector k. Here we consider the homogeneous case. The lighter regions of the figure correspond to where the occupied contribution from the spectral intensity is highest. The temperature here is chosen to be relatively high, around $1.9T_c$, in order to have some contribution to the RF current from pre-existing thermal fermionic excitations. The intensity map indicates upward and downward dispersing contributions. These correspond, to a good approximation, to the two RF transitions: to state 3 from state 2 with dispersion $(E_k + \mu)$ and $(-E_k + \mu)$, respectively, which are shown in figure 1. These are measured relative to the bottom of the band. The width of this contour plot comes exclusively from the incoherent terms γ and Σ_0. Here we have chosen to represent the latter by an imaginary constant (as in the cuprate literature) $\Sigma_0 = -i\Gamma_0$. Based on equation (29) and for illustrative purposes we take $\gamma = 0.25T_F$ and $\Gamma_0 = 0.1T_F$, with a small resolution broadening (typical of the experiment) as well.

One can see that the bulk of the current, even at this high temperature, is associated with the pair states which are broken in the process of the RF excitation. This figure describes in a conceptual way how this intensity map can be used to compare with a broadened BCS-like form [27, 74] for the spectral function. This form fits very well the two branches shown in the figure corresponding to upward and downward dispersing curves. In this way one can, in principle, establish the presence of pairing and extract the pairing gap size.

We stress that these calculations are for the homogeneous case and it is important to extend them to include the effects of a trap. This can be done within an LDA approximation scheme. Once the trap is included the simple analogy between the electronic ARPES experiments and momentum resolved photoemission spectroscopy is invalidated. However, many of the central features survive. While the two branches shown in the contour plot in figure 13 are, in principle, present, there is

a third new branch which appears as well. This corresponds to essentially free atoms at the trap edge which will contribute significantly [43, 45] to the RF current. It is this branch which is also upward dispersing which makes it rather difficult to see the effects of the pre-existing thermally broken pairs.

We summarize the results shown elsewhere [85] for the behavior of the occupied spectral intensity in a unitary trapped gas over a range of different temperatures. At high T, the central notable feature is a single upward dispersing curve which fits the free particle dispersion. This dispersion can be readily differentiated from that associated with pre-existing thermally broken pairs which varies as $E_k + \mu$ and, of course, depends on the distribution of energy gaps $\Delta(r)$. It arises from free atoms at the trap edge (where the gap $\Delta(r)$ is small). As the temperature is decreased toward T_c a second (downward dispersing) branch becomes evident. In the vicinity of the transition, the intensity map is bifurcated with two co-existing peaks: one coming from the free atoms at the trap edge and the second from the condensate pairs which are broken in the process of the RF excitation. The separation of the two peaks can be difficult to discern until k values are sufficiently high. Finally, at the lowest temperatures the striking feature is a single downward dispersing branch. This reflects the fact that essentially all atoms are now paired in the condensate. Just as in the homogeneous case discussed above, a BCS-like fit to this dispersion can be used to determine the pairing gap. We stress that there are no abrupt changes in the RF behavior at the superfluid transition, very much like what we saw earlier in our summary of the cuprate literature.

6. Analysis of theoretical and experimental RF spectra

6.1. Momentum resolved spectroscopy

We now compare theory and experiment in a trap based on the momentum resolved spectra previously discussed for the homogeneous case. In figure 14 we have taken a larger intrinsic broadening and included an empirical resolution broadening as well, again somewhat larger than the value indicated for the experiments. These parameters are seen to optimize semi-quantitative agreement with the data plotted in the top panel from [27].

The bottom panel presents the theoretical intensity maps. The dotted white curve represents a fit of the experimentally deduced peak dispersion while the solid white curve is the theoretical counterpart. Here, as in the experiment, we have fit the energy distribution curve to a *single* Gaussian peak. The comparison between the two white curves shows semi-quantitative consistency. Moreover, both the solid and the dotted white curves can be well fit to the BCS dispersion involving E_k, as was originally proposed in [76]. While figure 14 seems to capture the essential results shown in the experiment, with higher resolution it should be possible to obtain more direct information about the mean experimentally deduced gap size. Importantly, this reasonable agreement and the fact that the experiments were done near T_c suggest that there is a sizable pseudogap in the Fermi gases at and above T_c at unitarity.

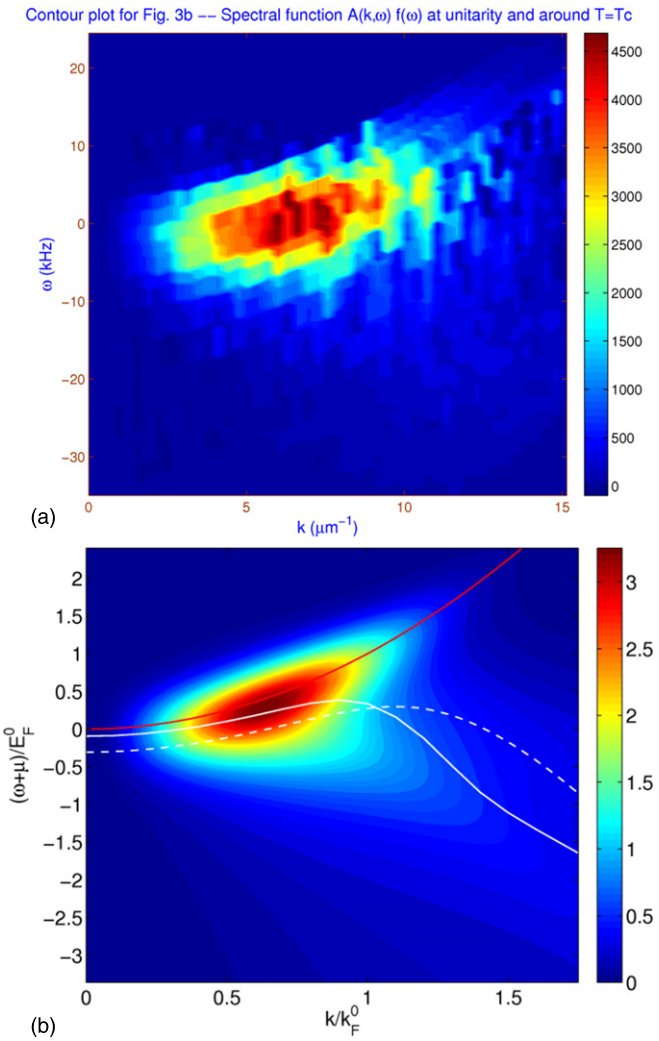

Figure 14. Contour plots of momentum resolved RF spectra in a trapped configuration. Top panel (*a*) is experimental data [27]. Reprinted by permission from Macmillan Publishers Ltd: *Nature* (**454** 744–7), copyright (1969). Theoretical results (*b*) correspond to occupied spectral intensity map, in a unitary trapped Fermi gas at $T/T_c = 1.1$. Here $\Sigma_0 = 0.35E_F^0$ and $\gamma = 0.38E_F^0$ at the trap center. The upper (red) curve represents the free atom dispersion, while the white solid and dashed curves are the quasi-particle dispersion obtained theoretically and experimentally [27], respectively, via fitting the energy distribution curves (EDCs) with a single Gaussian.

6.2. RF spectra in a trap

In figure 15 we show typical RF spectra in the trapped case. The figure indicates that there are two peaks at intermediate temperatures (top panel) and one peak at very low T (bottom panel). The interpretation of the former case has been in the literature since the early work in [42, 43, 45]: the zero detuning contribution comes from free atoms at the trap edge while the broad peak is associated with pairing. These theoretical observations have also been made recently [54] in the context of comparing the behavior in the homogeneous case (for which, evidently, no negative detuning peak was found in the normal phase) and the trapped cases. By contrast, within the present theoretical framework, a two peaked structure is predicted for a homogeneous gas as well [41, 52]. We have

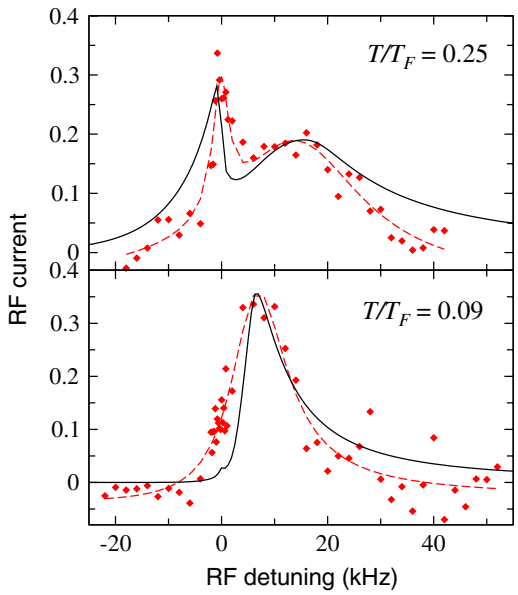

Figure 15. Comparison of calculated RF spectra of a trapped gas (solid curve, $T_c/T_F \approx 0.29$) with experiment [42] (symbols) in a harmonic trap calculated at 822 G for two (estimated) temperatures; from [45]. The dashed lines are a guide to the eye. There is reasonable agreement, but because final state effects are not included, the high frequency tails are overestimated in the theory.

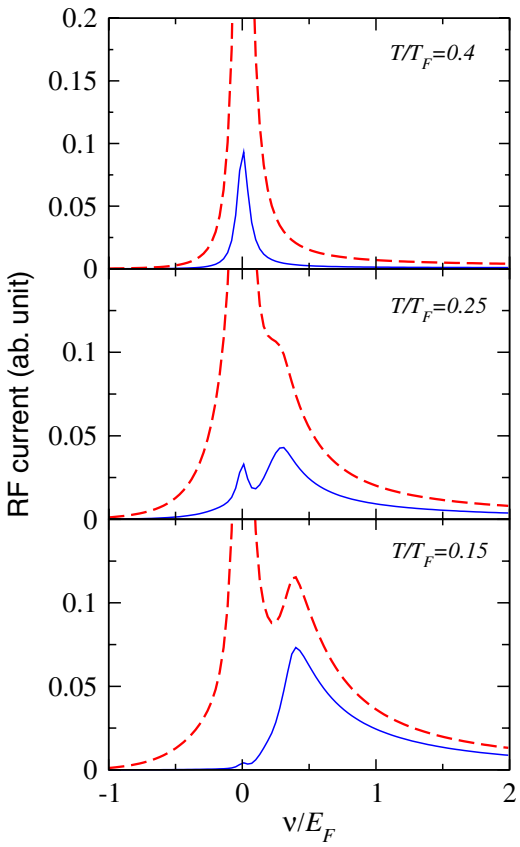

Figure 16. RF spectra for a trapped unitary imbalanced gas with $\delta = 0.5$. Here we take $\gamma/E_F^0 = 0.05$. Four different temperatures are indicated. Majority spectra are in (red) dashed lines and minority in (blue) solid lines.

seen that this negative peak is associated with thermally excited quasi-particles.

Figure 15 compares RF spectra in a trap near unitarity (solid curve) with experiments from [42] (symbols) at 822 G on ^{6}Li and for two different temperatures. The dashed curve is a fit to the data, serving as a guide to the eye. While the upper peak reflects the existence of pairing, it is not possible to directly infer the size of the (trap averaged) pairing gap Δ. However, it is now reasonably clear [15] that a pairing gap (pseudogap) is present in the normal state even in these early experiments from the Innsbruck group. The lower curve can be interpreted to suggest that the atoms at the trap edge have lower temperatures compared with $\Delta(r, T)$. The agreement between theory and experiment is not unreasonable for this leading order calculation (based on $I_0(\nu)$). One can, however, see that the theory in both cases shows a much slower drop-off with increasing high frequency than seen experimentally. We will see shortly that this difference is associated with final state effects.

In figure 16 we present similar RF spectra for [53] a trapped imbalanced gas near unitarity. The polarization is $\delta = 0.5$, and the spectra are plotted for three different temperatures. Here $T_c/T_F = 0.25$. It is useful to refer back to the lower right panel in figure 6 to see precisely what region of the polarized gas phase diagram is relevant. The red curves correspond to the majority and the blue to the minority. For the majority, one can see that the free atom peak at $\nu = 0$ is present at all temperatures, unlike the previous case in a balanced gas. At the highest temperature $T/T_F = 0.4$ (which is close to $T^*/T_F \approx 0.35$) the system is normal and pairing is absent. Very close to T_c in the middle panel one sees a clear pairing peak signature associated with the pseudogap. For this analysis we chose the broadening in equation (29), to be very small with $\gamma = 0.05 E_F$.

6.3. *Final state effects*

As we saw in figure 15, final state effects are expected to cut off the long tails in the RF spectra found theoretically in the lowest order theory. It has been argued [31] by the MIT group that one should limit the importance of these final state contributions by studying a unitary 1-3 superfluid instead, with an RF transition involving (for example) $3 \rightarrow 2$. For this case the magnitude of the final state scattering length is small, although it is positive. This will lead to a bound state contribution in the spectra, although it will not perceptibly change the shape of the continuum contributions. One could alternatively argue that it is better to work with the 1-2 superfluid where there are (generally) no bound states and where one can, more readily, impose the sum rules to arrive at estimates of the pairing gap. At this point both options should be explored.

In figure 17 we compare homogeneous spectra at $T = 0.15 T_F$ with and without final state effects for these two different superfluids at unitarity. All figures have been normalized to the same maximum value. The figure on the top corresponds to the configuration of the Innsbruck experiments [42] and on the bottom to recent MIT experiments [31]. It can be seen that final state effects in both cases do not change [47]

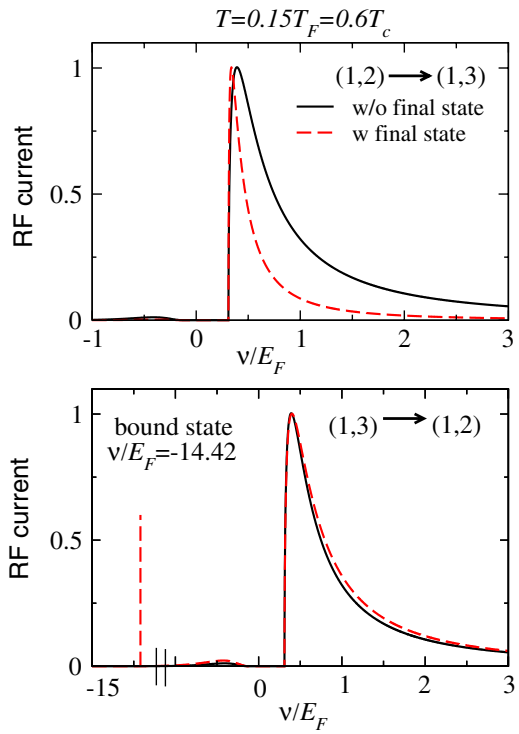

Figure 17. Comparison of homogeneous RF spectra of a unitary gas with (red, dashed) and without (black) final state effects at $T/T_{\rm F} = 0.15$. The top figure is for the 1-2 superfluid and the bottom is for the 1-3 case, showing a bound state. Calculations were done with $\gamma = 0$.

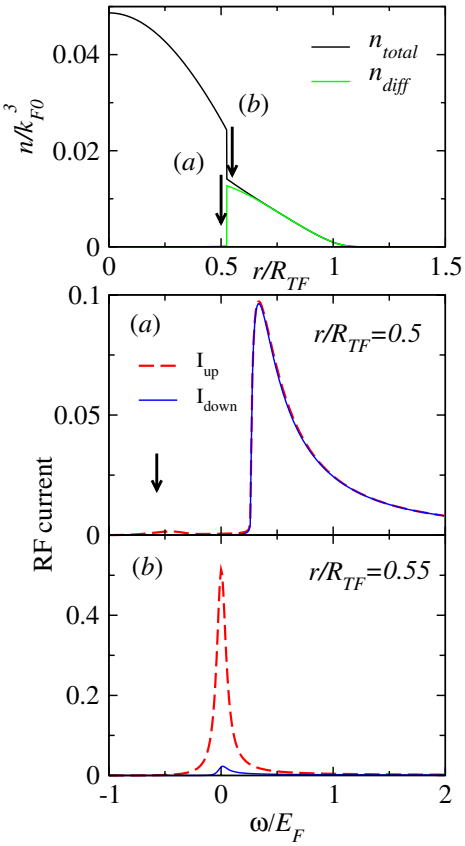

Figure 18. Homogeneous RF spectra of unitary, population imbalanced ($\delta = 0.5$) gas at very low $T/T_{\rm F} = 0.05$, where phase separation is stable. Upper panel is density profile indicating radii (a) and (b) used in lower two panels to compute the tomographic or homogeneous spectra. (Red) dashed lines are majority and (blue) solid lines are minority. No final state effects are included and we take $\gamma/E_{\rm F}^0 = 0.05$.

the threshold $\approx 0.4\Delta$ for the positive continuum (discussed in section 4). However, they do lead to a somewhat sharper peak and to a more rapid fall off at high detuning, as is consistent with the sum rules.

It is not easy to do the calculations which include final state effects in a trap so we can only qualitatively infer from the top panel in figure 17 that the corrections associated with their inclusion are what is needed to improve the agreement between theory and experiments on the 1-2 superfluid in figure 15. If final states introduced a bound–bound transition on the BCS side of resonance, as conjectured [31], it would probably not be sufficiently robust with respect to temperature [52], and would likely merge with the continuum with increasing T. Moreover, this positive continuum contribution is always present (provided, of course, that there is pairing); theoretically, one never finds simply an isolated bound–bound transition. With a small amount of lifetime broadening (γ) it is likely that a final state induced bound–bound transition on the BCS side of resonance would not make a noticeable difference. In this way, although some concern has been raised [31] about whether or not the Innsbruck experiments were properly interpreted as evidence for a pairing gap (rather than a possible bound–bound [51] transition), we concur with their original interpretation.

By contrast with the 1-2 superfluid, when final state effects for the 1-3 superfluid are included, there is little change in the shape of the spectra (shown on the bottom). There is, however, an important change of vertical scale associated with the bound state and related to the sum rule.

6.4. Tomographic scans in imbalanced gases

In figure 18 we turn to effectively homogeneous spectra associated with tomographic plots in the same imbalanced gas ($\delta = 0.5$) studied earlier. Here we consider extremely low temperatures so that [58] the system is in the phase separated state as can be seen from the lower right plot in figure 6. One can see this phase separation in the top panel which presents the density profiles. Also indicated are the two points (a) and (b) which establish the radii (used in the lower panels) at which the RF spectra are plotted. Here $R_{\rm TF} = \sqrt{2E_{\rm F}/m\omega^2}$ is the Thomas–Fermi radius and m and ω denote the fermion mass and trap frequency. The (red) dashed and (blue) solid curves are for the majority and minority, respectively. The middle panel shows that just inside the superfluid core there is very little difference in the majority and minority spectra as expected for a locally unpolarized superfluid. The lower panel shows the behavior just on the other side of the phase separation boundary where there is very little minority and hence very little pairing. As a consequence the RF peaks are close to zero detuning. We stress here that we are using the strict BCS-Leggett theory without including Hartree effects. With the latter included there may be a relative shift of the energy scales associated with the majority and minority atoms [64].

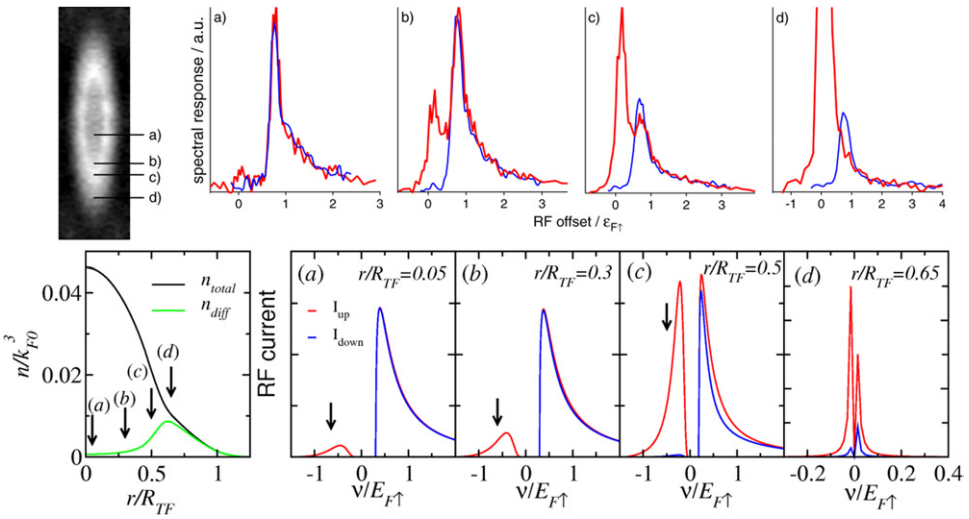

Figure 19. Comparison between theory and experiment [64] in top panel, for tomographic scans of an imbalanced unitary gas. Theory assumes $\delta = 0.5$, for definiteness. Here $T/T_F = 0.15$. The calculations are for a 1-3 superfluid (as in experiment) with final state effects included ($1/k_F a_{12} = 2.5$), and $\gamma = 0$. Light (red) indicates majority and dark (blue), minority. Hartree effects have not been included in theory and the horizontal scales are thus different. Arrows indicate the position of the gap. Here, following experiment we use the local Fermi energy of the majority atoms in the trap. In all other figures, E_F is used, corresponding to the bulk Fermi energy. Reprinted excerpt with permission from Schirotzek A *et al* 2008 *Phys. Rev. Lett.* **101** 140403. Copyright (2008) by the American Physical Society.

Figure 19 presents a comparison between theory (with final state effects) and experiment [64] at moderate temperatures ($T_c = 0.25T_F$) within the bulk Sarma phase. The theory and experiments are for the 1-3 superfluid at unitarity. The upper panel corresponds to recent data from MIT [64], indicating via a contour plot, the various radii probed in the tomographic scans. In the lower panel, the counterpart theoretical profile indicates four different radii via (a), (b), (c) and (d). Also shown in the theory by the arrows is where $-\Delta$ would be found within the negative continuum. One sees a reasonable correspondence between theory and experiment, except in the last panel at the largest radius. Here presumably there are polaron [54, 63] effects (a binding of a single minority spin to the bulk majority) which are not included in the calculations. We stress that additionally Hartree effects have not been included in the theory so that the zeros of the horizontal energy scales are not equivalent.

These Hartree effects have been extensively analyzed in [64]. Moreover, these authors have exploited a simple physical picture of the extreme low imbalance, low temperature behavior of the Sarma phase to argue that one can extract the size of the pairing gap Δ at unitarity from the maximum in the negative peak in these same data. In figure 20(*a*) we present tomography-based calculations implementing this procedure. Here we plot the spectra for various radii at very low temperatures, $T/T_F = 0.02$, and for very low polarization $\delta = 0.01$. The top inset shows a blow-up of the very small negative detuning peak while the bottom inset shows that the position of the maximum is, as conjectured, [64] very close to the actual gap size. A more realistic situation is outlined in figure 20(*b*) (lower panel) where the polarization has been raised to $\delta = 0.1$ and one can now detect the negative detuning peak more directly. Here one sees that there is roughly a 20% error in the estimate of the pairing peak size, compared with its actual value. This is consistent with the observations in previous figures as well. It is difficult to extrapolate to the nearly unpolarized case, say in the trap center, because as emphasized in figure 20(*a*), at low T and low δ the negative detuning peak simply cannot be detected. It does seem likely that errors of the order of 20% to, perhaps, 30% will be encountered when this procedure is implemented [64] to extract the gap size.

7. Photoemission experiments in the cuprates

We now turn to recent issues in photoemission experiments [86] in the underdoped cuprates. These call attention to the question of how the $\boldsymbol{k}$ dependence of the spectral function varies as one crosses T_c. These same issues may surface ultimately with momentum resolved RF spectroscopy [27], although it is only the magnitude of $\boldsymbol{k}$, rather than its angular dependence, which will be of interest. An earlier discussion on the cuprates in figure 3 focused on the $\boldsymbol{k}$ integrated photoemission spectra. As in this previous figure here we address how superconducting coherence is manifested when there is a normal state pseudogap. We stress that measurements like photoemission and RF spectroscopy are not phase sensitive probes of the system and cannot directly prove the existence of superfluidity.

We first focus on the region near the gap nodes, where the gap is smallest. The experiments of interest here very likely contain important clues as to the nature of the superconducting state which appears in the presence of a normal state pseudogap. While many aspects of the cuprates below T_c appear to be typical of (d-wave) BCS superconductors one expects some differences to appear simply because an excitation gap is present at the onset of superconductivity.

There are four key points which have been identified in [86]. We believe these are consistent with a BCS–BEC crossover interpretation of these cuprate photoemission data.

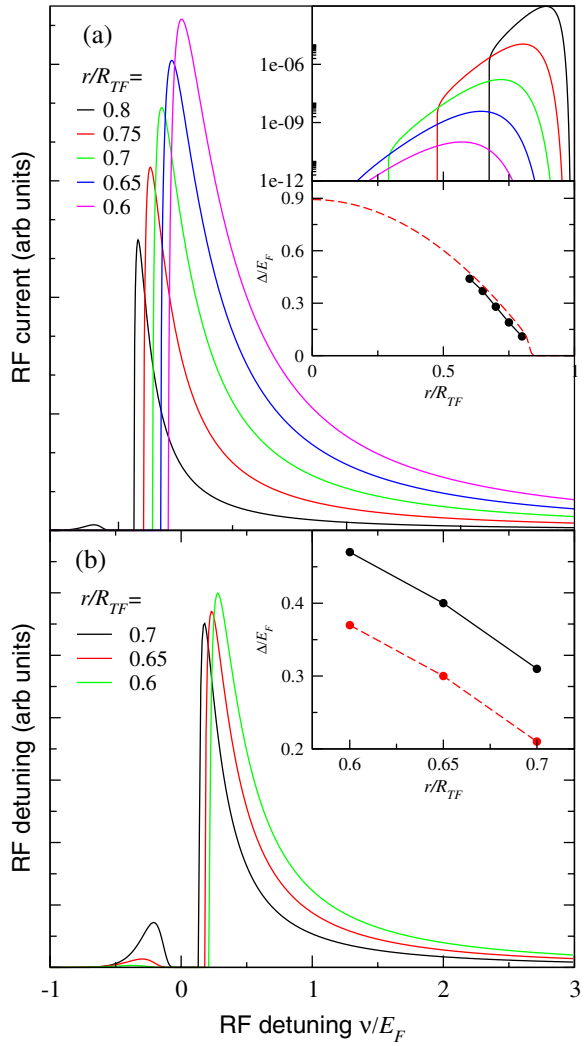

Figure 20. This figure addresses the feasibility of using the negative detuning peak to extract the pairing gap from a slightly polarized gas, following the suggestion in [64]. Panel (*a*) refers to the ideal case and the upper inset makes it clear that while the negative peak is at the gap frequency, it will be very difficult to detect for this a small polarization ($\delta = 0.01$). Panel (*b*) refers to a more moderate polarization ($\delta = 0.1$) where there will be roughly a 20% error in the gap as estimated this way. In both insets the (red) dashed and (black) solid curves correspond, respectively, to the precise theoretical results for Δ and to those inferred as described here.

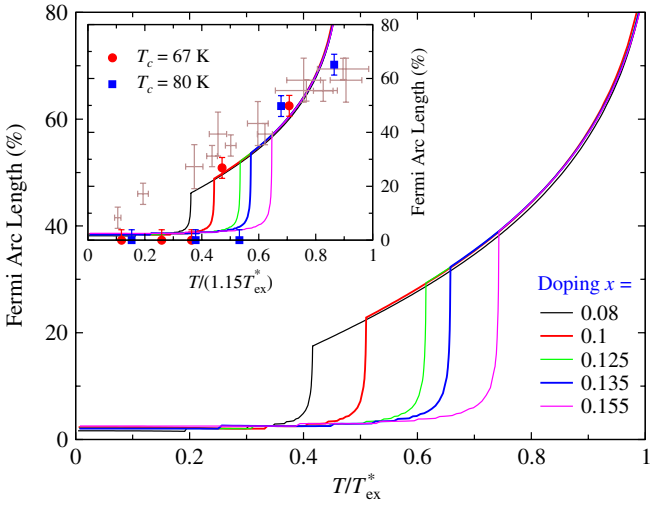

Figure 21. Fermi arc length as a function of T/T^*_{ex} for doping concentrations from optimal to underdoping for a cuprate superconductor. Fermi arc length is typically finite above T_c and drops to zero upon the onset of phase coherence. The normal state portions of the curves are close to universal, in agreement with [87]. The comparison in the inset between the theory with a slightly (15%) enlarged T^*_{ex} and experimental data (symbols) [86] shows a good semi-quantitative agreement. (Color online.)

As reported [86] (i) the excitation gap, $\Delta(\boldsymbol{k})$, as measured in photoemission experiments, remains roughly constant at temperatures from very low T to temperatures well above T_c. (ii) In the superfluid phase $\Delta(\boldsymbol{k})$ displays the expected point nodes (associated with d-wave symmetry); however, these rapidly broaden into Fermi arcs once the temperature reaches the vicinity of, and surpasses T_c. Importantly, 'this remarkable change occurs within the width of the resistive transition at T_c'. (iii) It has also been reported [87] that the energy scale associated with the excitation gap appears to be T^*, which is conventionally taken as the pseudogap [14, 15, 22] onset temperature, and that the Fermi arc length scales with T/T^* above T_c. From (i) it is inferred that (iv) 'the energy gap is *not* directly related to the superconducting order parameter'.

To address these and other photoemission experiments, the normal state self-energy is taken [44, 78, 79] to be of the form shown in equation (29) with equation (27) and with a purely imaginary background self-energy: $\Sigma_0(\boldsymbol{k}, \omega) = -\mathrm{i}\Gamma_0$. Although it is not a necessary assumption, it is widely assumed [78] that Γ_0 should be same as γ. The rapid, but smooth destruction of the d-wave point nodes as temperature is raised can be physically associated with the fact that the superconducting order parameter Δ_{sc} disappears smoothly but precisely at T_c. Above T_c the effects of γ and Σ_0 lead to a smearing and the point nodes are replaced by Fermi arcs [78]. Below T_c with the onset of phase coherence through Δ_{sc}, the arcs are rapidly replaced by point nodes. One says that there has been 'a collapse of the Fermi arcs', and that the nodes are 'protected' below T_c.

The collapse is a continuous process. We argue that it is not to be associated with a disappearance of the inverse lifetime γ, but rather it reflects the gradual emergence of the condensate to which the finite momentum pairs are continuously converted as T decreases. This is related to the fact that, from equation (27), we see there are two terms in the self-energy below T_c. At the lowest temperatures Δ_{pg} vanishes, whereas above T_c, it follows that Δ_{sc} is zero.

In figure 21 we address these new experiments by showing the collapse of the Fermi arcs from above to below T_c within the same general BCS–BEC crossover formalism as was used for the cold gases. We plot the percentage of Fermi arc length as a function of T/T^* and for different doping concentrations from the optimal ($T^* \approx T_c$) to the underdoped regime ($T^* \gg T_c$). The observed collapse is intimately connected with our earlier observation that the spectral function in equation (30) has a zero at $\omega = -\xi_{\boldsymbol{k}}$ below T_c, whereas the spectral function has no zero above T_c.

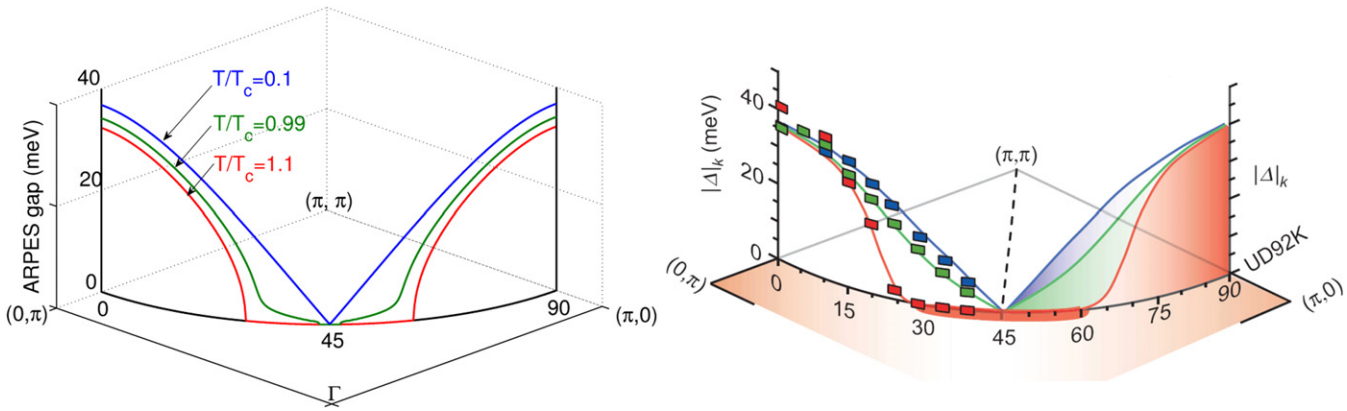

Figure 22. Contrasting nodal and anti-nodal temperature dependences in the d-wave case. Figure on the left is the ARPES gap as a function of angle ϕ at $T/T_c = 1.1, 0.99, 0.1$ (labeled on the figure). This figure should be compared with the experimental plots on the right taken from figure 5 in [88]. Reprinted with permission from Macmillan Publishers Ltd: *Nature* (**450** 81), copyright (2007).

There has been a recent emphasis on a related class of experiments which contrasts the behavior around the gap nodes with that around the gap maxima (or anti-nodes). The right hand panel of figure 22 indicates the size of the ARPES or spectral gap as deduced from one-half of the peak to peak separation in the spectral function. These data [88] address a moderately underdoped sample. The three different curves correspond to three different temperatures with the legend the same as that in the left hand panel (representing the results of BCS–BEC crossover theory). Importantly, one sees a pronounced temperature dependence in the behavior of the ARPES spectral gap for the nodal region (near 45°), as compared with the anti-nodal region (near 0 and 90°), where there is virtually no T dependence.

Theory (on the left) and experiment (on the right) are in reasonable agreement and one can readily understand the contrasting temperature response associated with the different $\boldsymbol{k}$ points on the Fermi surface. To see this, note that the nodal regions reflect extended gapless states or Fermi arcs [86] above T_c. It is natural to expect that they are sensitive to the onset of Δ_{sc}, in the same way that a strict BCS superconductor (which necessarily has a gapless normal state) is acutely sensitive to the presence of order. By contrast, the anti-nodal points are not so affected by passing through T_c because they already possess a substantial pairing gap in the normal phase.

The dramatic variation in the temperature dependence of the spectral gap as one moves along the Fermi surface has given rise to the so-called 'two-gap scenario' [18]. In (perhaps) overly simplistic terms the one-gap and two-gap scenarios are differentiated by the presumption that in the former the pseudogap represents a precursor to superconductivity, while in the latter the mysterious cuprate pseudogap is viewed as arising from a competing order parameter. The two-gap scenario is viewed as a consequence of a number of different experiments [18, 89] all of which have been interpreted to suggest that the anti-nodal region is associated with this alternative (hidden) order parameter pseudogap and the nodal region is dominated by superconductivity. By contrast, the viewpoint expressed here (based on BCS–BEC crossover theory) leads naturally to a different T dependence for the nodal and anti-nodal region, but at the same time it belongs to the class of theories which argue that the pseudogap is intimately connected with the superconductivity.

We believe that the reasonable agreement between theory and experiment shown in these last two plots supports our physical picture that pseudogap effects derive from the superconductivity itself and are a consequence of a stronger-than-BCS attractive interaction. There are 'two-gap' like features which are present in the ARPES or spectral function temperature dependences. These two-gap components are to be associated with the non-condensed pair excitations which are distinguishable from the condensate. The presence of pseudogap contributions below T_c is a crucial consequence of BCS–BEC crossover and reflects the fact that pre-formed pairs above T_c do not abruptly disappear just below T_c.

In summary, with this recent class of photoemission observations has come a recognition that the superfluid phase in the cuprates is, itself, very complex and has to be distinguished from a simple BCS d-wave superconductor. At the very least an important difference between the cuprates and strict BCS theory is the presence of a large excitation gap at the temperature of condensation. We also reiterate that this purportedly more complex superfluid, containing non-condensed pair excitations, can potentially be elucidated through studies of BCS–BEC crossover in the cold Fermi gases.

8. Conclusions

There has been enormous progress in the field of radio frequency (RF) spectroscopy of the Fermi gases. This technique holds promise of being as valuable to these atomic superfluids as photoemission has been to the cuprates. We have tried in this review to argue that it also holds promise of helping to address some fundamental issues in the cuprates which are very general, such as how to describe that anomalous superfluid phase which forms in the presence of a normal state excitation gap.

On a less general level, these RF experiments also hold promise of helping to address (that is, support or rule out) one particular approach to the theory of high temperature

superconductivity: namely that based on BCS–BEC crossover. There are many alternative physical pictures of the cuprates and, indeed, the ultracold gases on optical lattices have presented themselves as possible simulators of at least some of these alternatives. Most notable among these are the proposed cold gas studies of the repulsive Hubbard model which is thought to be relevant to the 'Mott physics' aspects of the high T_c superconductors.

A goal of this review was to present a broad background to the theory of RF spectroscopy and its relation to photoemission spectroscopy. We summarize key experiments using both techniques and show how they can be addressed within a BCS–BEC crossover approach. Included in our analysis are trapped as well as homogeneous gases and population imbalanced gases. The RF field has seen a proliferation of methodologies including tomographic and momentum resolved scans, all of which are discussed here.

The immediate excitement surrounding these RF experiments is in large part because they hold the potential for measuring the pairing gap Δ. As time passes, however, it has become progressively more clear that extracting detailed quantitative information is increasingly difficult. There is no signature in the RF spectra of Δ except to establish whether it is present or not. This observation applies to both balanced and imbalanced gases. Here we summarized three methodologies which might make it possible to extract more precise numerical values for Δ: either through sum rules which involve integrals of the measured RF spectra, through recent momentum resolved experiments or by the use of imbalanced gases. The first and the third of these make further use of enhancing the negative detuning continuum either by imbalance or by final state effects. At this moment, only the last of these has been put into experimental practice [64] at a quantitative level.

Our analyses (and all results presented in this paper) are subject to the caveat that they are obtained within the BCS-Leggett crossover theory (extended to finite T). This theory, like all others is not an exact theory. However, this approach to the crossover is one which is particularly well suited to the cuprates because there are no spurious first order transitions. Recently, there have been RF calculations based on an alternative scheme [50, 54] which is closer to the Nozieres–Schmitt-Rink approach to BCS–BEC crossover. This is very nice work, which we have only briefly mentioned, which addresses radio frequency experiments in the normal state and at $T \approx 0$. The latter, in particular, has been important in elucidating how to incorporate final state effects. We also only make passing reference to the body of work on the highly imbalanced gases.

It should be clear that this field is moving rapidly and much has been accomplished at the theoretical and experimental ends. However, in writing this review, we felt it was timely to suggest possible new directions for cold gas research which might elucidate the cuprate superconductors. As summarized earlier, the key issues which have emerged in photoemission studies involve characterization of the fermionic self-energy, of the pseudogap and of the signatures of superconducting coherence (in passing from above to below T_c). These issues have a counterpart in the ultracold Fermi gases as we have suggested here and it will be of enormous benefit in future to exploit this new class of 'materials' to address these fundamental questions in condensed matter.

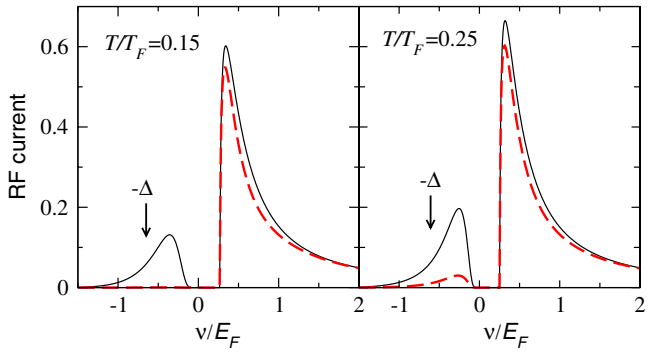

Figure 23. RF current of the unitary polarized ($\delta = 0.1$) gas at $T = 0.15T_F$ and $T = 0.25T_F$. For these temperatures, the Sarma state is stable. The (black) solid curve is for the majority and (red) dashed is for the minority. The arrows indicate the position of $-\Delta$. $T_c \approx 0.24T_F$ in this case.

Acknowledgments

This work is supported by NSF PHY-0555325 and NSF-MRSEC Grant 0820054. The authors thank Cheng Chin, Debbie Jin, Jayson Stewart, John Gaebler, W Ketterle, E Mueller and D Wulin for many useful communications and conversations.

Appendix A. Analytical results for RF spectra in homogeneous, polarized gas

Following the same arguments as in section 3.5, for the polarized case, we have for the majority current

$$I_0^{(1)}(\nu) = \frac{1}{8\pi^2}\frac{\Delta^2}{\nu^2}k_0[1 - f(E_0 + h)], \qquad (\nu > \nu_1), \quad \text{(A1)}$$

$$I_0^{(1)}(\nu) = \frac{1}{8\pi^2}\frac{\Delta^2}{\nu^2}k_0 f(E_0 - h), \qquad (\nu_2 < \nu < 0) \quad \text{(A2)}$$

and the minority RF current

$$I_0^{(2)}(\nu) = \frac{1}{8\pi^2}\frac{\Delta^2}{\nu^2}k_0[1 - f(E_0 - h)], \qquad (\nu > \nu_1), \quad \text{(A3)}$$

$$I_0^{(2)}(\nu) = \frac{1}{8\pi^2}\frac{\Delta^2}{\nu^2}k_0 f(E_0 + h), \qquad (\nu_2 < \nu < 0). \quad \text{(A4)}$$

Here $\mu = (\mu_\uparrow + \mu_\downarrow)/2$ is the average chemical potential and $h = \mu_\uparrow - \mu_\downarrow$ is the chemical potential difference. Since $E_0 + h$ is always positive, the minority RF current is not associated with a negative continuum at low temperatures. On the other hand, since generally $E_0 - h < 0$, the majority RF current has a negative continuum. For strictly zero temperature, the negative continuum is located in the range $-h - \sqrt{h^2 - \Delta^2} < \nu < -h + \sqrt{h^2 - \Delta^2}$. In figure 23, we show the RF current for the stable Sarma state for small population imbalance $\delta = 0.1$. We note that the negative peak location is not at $-\Delta$.

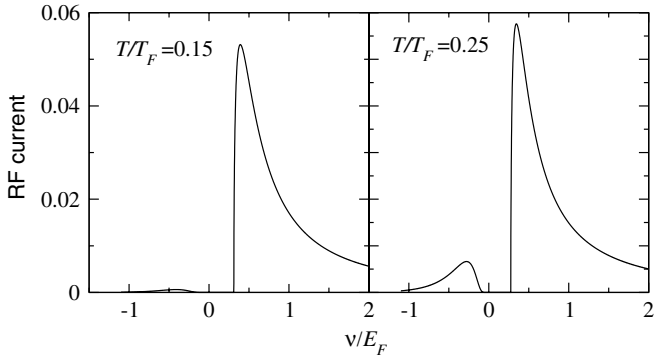

Figure 24. RF current of the unitary unpolarized gas at $T = 0.15T_{\rm F}$ and $T = 0.25T_{\rm F}$. $T_{\rm c} = 0.255T_{\rm F}$ in this case. This figure is included as a contrast to the polarized case, to make it evident that the negative continuum is more difficult to see in the absence of polarization.

In figure 24 we compare with the unpolarized case, showing that there is essentially no negative continuum (until one approaches temperatures closer to $T_{\rm c}$). We can ask why the onset of the negative continuum is unrelated to the energy scale Δ. The answer is that while the negative continuum in the Sarma phase is associated with the presence of excess fermions (as seen by comparing the two figures in this appendix), these excess fermions in the Sarma phase are essentially gapless. Thus, they are not directly associated with an energy scale which involves Δ in any explicit way.

Appendix B. Details on the final state effect diagrams

The response function which yields the RF current is

$$D(\nu) = D_0(\nu) + D_2^2(\nu)\, t_{13}(\nu), \tag{B1}$$

where the first term is the usual leading order contribution and the second corresponds to the Aslamazov–Larkin (AL) diagram given by

$$\begin{aligned} D_{\rm AL}(Q) = &- \sum_{K,K',P} G^{(2)}(K) G_0^{(1)}(-K) G_0^{(3)}(K+Q) \\ &\times t_{12}(P) G^{(2)}(K') G_0^{(1)}(-K') G_0^{(3)}(K'+Q) t_{13}(Q) \\ = &\left[\Delta \sum_K G(K) G_0(-K) G_0^{(3)}(K+Q)\right]^2 t_{13}(Q), \end{aligned} \tag{B2}$$

where, as discussed in the text, we have $t_{12}(Q) \approx -\Delta^2 \delta(Q)/T$. This term can be rewritten in terms of the functions $F(Q)$ and $D_2(Q)$ defined in the main text. We introduce the RF detuning frequency ν:

$$i\Omega \to \Omega + i0^+ = \nu + \mu_2 - \mu_3 + i0^+. \tag{B3}$$

The retarded form of the various complex functions which enter into the RF current can be summarized as

$$\begin{aligned} D_0^{\rm R}(\nu) = \sum_k \Bigg[&\frac{f(E_k) - f(\xi_{k,3})}{\nu + E_k - \xi_k + i0^+} u_k^2 \\ &+ \frac{1 - f(E_k) - f(\xi_{k,3})}{\nu - E_k - \xi_k + i0^+} v_k^2 \Bigg], \end{aligned} \tag{B4}$$

$$\begin{aligned} D_2^{\rm R}(\nu) = \sum_k \frac{\Delta}{2E_k} \Bigg[&\frac{1 - f(E_k) - f(\xi_{k,3})}{\nu - E_k - \xi_k + i0^+} \\ &- \frac{f(E_k) - f(\xi_{k,3})}{\nu + E_k - \xi_k + i0^+} \Bigg], \end{aligned} \tag{B5}$$

$$\begin{aligned} \chi_{13}^{\rm R}(\nu) = -\sum_k \Bigg[&\frac{1 - f(E_k) - f(\xi_{k,3})}{\nu - E_k - \xi_k + i0^+} u_k^2 \\ &+ \frac{f(E_k) - f(\xi_{k,3})}{\nu + E_k - \xi_k + i0^+} v_k^2 + \frac{1}{2\epsilon_k} \Bigg]. \end{aligned} \tag{B6}$$

To compute the RF current, we calculate the real and imaginary parts of the above quantities. For later convenience, we introduce the following expressions:

$$\begin{aligned} B(\nu) = &\sum_k \frac{1}{2E_k} \Big[\frac{1 - f(E_k) - f(\xi_{k,3})}{\nu - E_k - \xi_k} - \frac{f(E_k) - f(\xi_{k,3})}{\nu + E_k - \xi_k} \Big], \end{aligned} \tag{B7}$$

$$\begin{aligned} C(\nu) = &-\pi \sum_k \frac{1}{2E_k} \{ [1 - f(E_k) - f(\xi_{k,3})] \delta(\nu - E_k - \xi_k) \\ &- [f(E_k) - f(\xi_{k,3})] \delta(\nu + E_k - \xi_k) \}. \end{aligned} \tag{B8}$$

We also define $B(\nu = 0) \equiv B(0)$ and $C(\nu = 0) \equiv C(0)$. For the most part it will be convenient to drop the argument and simply write B, C.

It can be shown that

$$\mathrm{Im} D_0^{\rm R} = \frac{\Delta^2}{\nu} C, \tag{B9}$$

$$\mathrm{Im} D_2^{\rm R} = \Delta C, \tag{B10}$$

$$\mathrm{Re} D_2^{\rm R} = \Delta B. \tag{B11}$$

We notice that

$$\begin{aligned} \chi_{13}(\nu) - \chi_{13}(0) = &-\nu \sum_k \frac{1}{2E_k} \Bigg[\frac{1 - f(E_k) - f(\xi_{k,3})}{\nu - E_k - \xi_k} \\ &- \frac{f(E_k) - f(\xi_{k,3})}{\nu + E_k - \xi_k} \Bigg] = -B\nu. \end{aligned} \tag{B12}$$

We make use of the 1, 2 superfluid gap equation and identify $\chi_{12}(0) = \chi_{13}(0)$, so that

$$\begin{aligned} \mathrm{Re}\, t_{13}^{-1,{\rm R}} &= \frac{m}{4\pi a_{13}} - \frac{m}{4\pi a_{12}} + \chi_{13}(\nu) - \chi_{13}(0) \\ &= \frac{m}{4\pi a_{13}} - \frac{m}{4\pi a_{12}} - B\nu, \end{aligned} \tag{B13}$$

$$\mathrm{Im}\, t_{13}^{-1,{\rm R}} = \mathrm{Im}[\chi_{13}^{\rm R}(\nu) - \chi_{13}(0)] = -C\nu - B\, 0^+. \tag{B14}$$

In the general case with $a_{12} \neq a_{13}$, it follows that

$$\begin{aligned} \mathrm{Im}\, D^{\rm R}(\nu) = \mathrm{Im}\, D_0^{\rm R} \\ + \frac{-\mathrm{Re}\,(D_2^{\rm R})^2 \mathrm{Im}\, t_{13}^{-1,{\rm R}} + \mathrm{Im}\,(D_2^{\rm R})^2\, \mathrm{Re}\, t_{13}^{-1,{\rm R}}}{(\mathrm{Re}\, t_{13}^{-1,{\rm R}})^2 + (\mathrm{Im}\, t_{13}^{-1,{\rm R}})^2}. \end{aligned}$$

After a straightforward calculation we have

$$\text{Numerator} = \frac{\Delta^2}{\nu} C \left(\frac{m}{4\pi a_{13}} - \frac{m}{4\pi a_{12}} \right)^2. \tag{B15}$$

In this way we rewrite the response function in the form presented in the text as

$$\text{Im}\, D^{\text{R}}(\nu) = \left(\frac{m}{4\pi a_{13}} - \frac{m}{4\pi a_{12}} \right)^2 \frac{\text{Im}\, D_0^{\text{R}}(\nu)}{|t_{13}^{-1,\text{R}}(\nu)|^2}. \tag{B16}$$

Appendix C. Special case of equal interactions

In the special case $a_{12} = a_{13}$, we expect $I(\nu) \propto \delta(\nu)$. We showed above that $\text{Im}\, t_{13}^{-1,\text{R}} = -C\nu - B\, 0^+$. The second term plays essentially no role in the $a_{12} \neq a_{13}$ case, but it is important in this special case. Combined with the real part, we have

$$t_{13}^{\text{R}} = -\frac{1}{(B + \text{i}C)\nu + \text{i}B\, 0^+}. \tag{C1}$$

Using the fact that $C = 0$ (when $a_{12} = a_{13}$), we find

$$\text{Re}\, t_{13} = -\frac{1}{\nu} \frac{B}{B^2 + C^2}, \tag{C2}$$

$$\text{Im}\, t_{13} = \frac{1}{\nu} \frac{C}{B^2 + C^2} + \frac{\pi}{B} \delta(\nu). \tag{C3}$$

Thus we have

$$\begin{aligned} \text{Im}\, D^{\text{R}}(\nu) &= \text{Im}\, D_0^{\text{R}}(\nu) + \text{Re}\, D_2^2\, \text{Im}\, t_{13}^{\text{R}} + \text{Im}\, D_2^{2,\text{R}}\, \text{Re}\, t_{13}^{\text{R}} \\ &= \pi \Delta^2 B\, \delta(\nu). \end{aligned} \tag{C4}$$

In the limit $a_{12} = a_{13}$

$$\begin{aligned} \Delta^2 B(0) = &-\sum_k \{[1 - f(E_k) - f(\xi_{k,3})] v_k^2 \\ &+ [f(E_k) - f(\xi_{k,3})] u_k^2\} = -(n_2 - n_3). \end{aligned} \tag{C5}$$

Thus we deduce

$$I(\nu) = -\frac{1}{\pi} \text{Im}\, D^{\text{R}}(\nu) = (n_2 - n_3)\delta(\nu), \tag{C6}$$

which is the expected [47] result.

Appendix D. Details on explicit evaluation of sum rules

We will next prove the sum rules on the zeroth and first moment of the RF spectra for the unpolarized case. We focus on the general case $a_{12} \neq a_{13}$. In the large ν limit, from equations (B7) and (B8) it follows that $B \sim \nu^{-1/2}$ and $C \sim \nu^{-1/2}$. Thus we have $\chi_{13}(\nu) = \chi_{13}(0) - B\nu \sim \nu^{1/2}$ as $\nu \to \infty$. We deduce $t_{13}(\nu) = [1/g_{13} + \chi_{13}(\nu)]^{-1} \sim \nu^{-1/2}$. Thus we have $I_0 \sim \nu^{-3/2}$ and $I \sim \nu^{-5/2}$ as $\nu \to \infty$. Consequently, we see that final state effects convert a diverging first moment into a finite result for the clock shift.

To obtain this shift quantitatively, we use the Kramers–Kronig relations for t_{13}.

$$\text{Re}\, t_{13}^{\text{R}}(\nu) = -\int_{-\infty}^{+\infty} \frac{\text{d}\nu'}{\pi} \frac{\text{Im}\, t_{13}^{\text{R}}(\nu')}{\nu - \nu'}. \tag{D1}$$

For convenience we define $\delta g = \frac{m}{4\pi a_{13}} - \frac{m}{4\pi a_{12}}$ so that

$$\text{Re}\, t_{13}^{\text{R}}(\nu) = \frac{\delta g - B\nu}{(\delta g - B\nu)^2 + (C\nu)^2}.$$

Then from the Kramers–Kronig relations with $\nu = 0$ we have

$$\int_{-\infty}^{+\infty} \frac{\text{d}\nu'}{\pi} \frac{\text{Im}\, t_{13}^{\text{R}}(\nu')}{\nu'} = \text{Re}\, t_{13}^{\text{R}}(0) = \delta g^{-1}. \tag{D2}$$

We also have by taking a derivative and setting $\nu = 0$,

$$\int_{-\infty}^{+\infty} \frac{\text{d}\nu'}{\pi} \frac{\text{Im}\, t_{13}^{\text{R}}(\nu')}{\nu'^2} = \frac{\partial}{\partial \nu} \text{Re}\, t_{13}^{\text{R}}(0) = B(0)/\delta g^2. \tag{D3}$$

From these results we can prove the sum rule:

$$\begin{aligned} \int \text{d}\nu I(\nu) &= -\delta g^2 \Delta^2 \int \frac{\text{d}\nu}{\pi} \frac{\text{Im}\, t_{13}^{\text{R}}(\nu)}{\nu^2} \\ &= -B(0)\Delta^2 = n_2 - n_3. \end{aligned} \tag{D4}$$

Then the first moment is

$$\begin{aligned} \int \text{d}\nu\, \nu I(\nu) &= -\delta g^2 \Delta^2 \int \frac{\text{d}\nu}{\pi} \frac{\text{Im}\, t_{13}^{\text{R}}(\nu)}{\nu^2} \\ &= -\delta g \Delta^2 = \Delta^2 \frac{m}{4\pi} \left(\frac{1}{a_{12}} - \frac{1}{a_{13}} \right). \end{aligned} \tag{D5}$$

Combining these equations we find for the mean clock shift

$$\bar{\nu} = \frac{\int \text{d}\nu\, \nu I(\nu)}{\int \text{d}\nu\, I(\nu)} = \frac{\Delta^2}{n_2 - n_3} \frac{m}{4\pi} \left(\frac{1}{a_{12}} - \frac{1}{a_{13}} \right), \tag{D6}$$

which is the expected result [47]. In the text we explore how this sum rule may be used to measure the pairing gap.

Appendix E. Final state effects in a homogeneous but polarized system

In the polarized case, states 1 and 2 have different chemical potentials. All the calculations will closely parallel the unpolarized case. In the following, we only consider the RF transition from state 2 to 3. The formulae for the transition from state 1 to 3 can be similarly derived. As before, we define

$$\begin{aligned} F'(K) &= -\Delta G^{(2)}(K) G_0^{(1)}(-K) \\ &= -\Delta \frac{1}{\text{i}\omega - \xi_k - h} \frac{-\text{i}\omega + \xi_k + h}{(\text{i}\omega - h)^2 - E_k^2} \\ &= \frac{\Delta}{(\text{i}\omega - h)^2 - E_k^2}. \end{aligned} \tag{E1}$$

Here $\mu = (\mu_\uparrow + \mu_\downarrow)/2$ and $h = (\mu_\uparrow - \mu_\downarrow)/2$.

Generalizing $D_2(Q)$ to the polarized case we find

$$\begin{aligned} D_2'(Q) = \sum_k \frac{\Delta}{2E_k} \Bigg[&\frac{1 - f(E_{k,\uparrow}) - f(\xi_{k,3})}{(\text{i}\Omega + h) - E_k - \xi_{k,3}} \\ &- \frac{f(E_{k,\downarrow}) - f(\xi_{k,3})}{(\text{i}\Omega + h) + E_k - \xi_{k,3}} \Bigg] \end{aligned}$$

with $E_{k,\uparrow} = E_k - h$ and $E_{k,\downarrow} = E_k + h$.

We analytically continue along with a shift of variables to write

$$i\Omega \to \Omega + i0^+ = \nu + \mu_2 - \mu_3 + i0^+. \tag{E2}$$

In this way we find the denominator in $D_2(Q)$ is the same as for the unpolarized case; the only difference is in the numerator.

$$1 - f(E_k) - f(\xi_{k,3}) \to 1 - f(E_{k,\uparrow}) - f(\xi_{k,3}),$$

$$f(E_k) - f(\xi_{k,3}) \to f(E_{k,\downarrow}) - f(\xi_{k,3}).$$

We can similarly evaluate $D_0(\nu)$ and $\chi_{13}(\nu)$. Finally, we note that

$$\mathrm{Im}\, D_0'^{\mathrm{R}} = \frac{\Delta^2}{\nu} C_2, \tag{E3}$$

$$\mathrm{Re}\, t_{13}'^{-1,\mathrm{R}} = \frac{m}{4\pi a_{13}} - \frac{m}{4\pi a_{12}} - B_2 \nu, \tag{E4}$$

$$\mathrm{Im} t_{13}'^{-1,\mathrm{R}} = -C_2 \nu \tag{E5}$$

with

$$B_2(\nu) \sum_k \frac{1}{2E_k} \left[\frac{1 - f(E_{k,\uparrow}) - f(\xi_{k,3})}{\nu - E_k - \xi_k} - \frac{f(E_{k,\downarrow}) - f(\xi_{k,3})}{\nu + E_k - \xi_k} \right],$$

$$C_2(\nu) = -\pi \sum_k \frac{1}{2E_k} \{ [1 - f(E_{k,\uparrow}) - f(\xi_{k,3})] \delta(\nu - E_k - \xi_k) - [f(E_{k,\downarrow}) - f(\xi_{k,3})] \delta(\nu + E_k - \xi_k) \}.$$

In this way we find for the RF current of state 2

$$I_2(\nu) = -\frac{1}{\pi} \left(\frac{m}{4\pi a_{13}} - \frac{m}{4\pi a_{12}} \right)^2 \frac{\mathrm{Im} D_0'^{\mathrm{R}}(\nu)}{|t_{13}'^{-1,\mathrm{R}}(\nu)|^2},$$

which is formally the same result we found in the absence of population imbalance. These results can readily be generalized to compute the current in state 1.

Appendix E.1. Sum rules for the polarized case

Just as for the unpolarized case, we have the Kramers–Kronig relations (D1) for t_{13}^{R}. Following the same analysis as for the unpolarized case we have

$$\int_{-\infty}^{+\infty} \frac{\mathrm{d}\nu'}{\pi} \frac{\mathrm{Im}\, t_{13}'^{\mathrm{R}}(\nu')}{\nu'} = 1/\delta g,$$

$$\int_{-\infty}^{+\infty} \frac{\mathrm{d}\nu'}{\pi} \frac{\mathrm{Im}\, t_{13}'^{\mathrm{R}}(\nu')}{\nu'^2} = B_2(0)/\delta g^2.$$

Now using the fact that $\Delta^2 B_2(0) = -(n_2 - n_3)$, it is straightforward to obtain the zeroth and first moment of the RF current:

$$\int \mathrm{d}\nu I_2(\nu) = n_2 - n_3,$$

$$\int \mathrm{d}\nu \nu\, I_2(\nu) = -\delta g \Delta^2.$$

Then the average clock shift is

$$\bar{\nu} = \frac{\int \mathrm{d}\nu\, \nu I_2(\nu)}{\int \mathrm{d}\nu\, I_2(\nu)} = \frac{\Delta^2}{n_2 - n_3} \frac{m}{4\pi} \left(\frac{1}{a_{12}} - \frac{1}{a_{13}} \right).$$

Again, this is, formally, the same as for the unpolarized case.

References

[1] Greiner M, Regal C A and Jin D S 2003 *Nature* **426** 537
[2] Jochim S *et al* 2003 *Science* **302** 2101
[3] Regal C A, Greiner M and Jin D S 2004 *Phys. Rev. Lett.* **92** 040403
[4] Zwierlein M W, Stan C A, Schunck C H, Raupach S M F, Kerman A J and Ketterle W 2004 *Phys. Rev. Lett.* **92** 120403
[5] Zwierlein M W, Abo-Shaeer J R, Schirotzek A and Ketterle W 2005 *Nature* **435** 170404
[6] Kinast J, Hemmer S L, Gehm M E, Turlapov A and Thomas J E 2004 *Phys. Rev. Lett.* **92** 150402
[7] Bartenstein M, Altmeyer A, Riedl S, Jochim S, Chin C, Denschlag J H and Grimm R 2004 *Phys. Rev. Lett.* **92** 203201
[8] Kinast J, Turlapov A, Thomas J E, Chen Q J, Stajic J and Levin K 2005 *Science* **307** 1296
[9] Bourdel T, Khaykovich L, Cubizolles J, Zhang J, Chevy F, Teichmann M, Tarruell L, Kokkelmans S J and Salomon C 2004 *Phys. Rev. Lett.* **93** 050401
[10] Partridge G B, Strecker K E, Kamar R I, Jack M W and Hulet R G 2005 *Phys. Rev. Lett.* **95** 020404
[11] Chin C, Grimm R, Julienne P and Tiesinga E 2008 arXiv:0812.149
[12] Giorgini S, Pitaevskii L P and Stringari S 2008 *Rev. Mod. Phys.* **80** 1215
[13] Bloch I, Dalibard J and Zwerger W 2008 *Rev. Mod. Phys.* **80** 885
[14] Chen Q J, Stajic J, Tan S N and Levin K 2005 *Phys. Rep.* **412** 1
[15] Levin K and Chen Q 2007 *Ultra-cold Fermi Gases* ed M Inguscio *et al* (Amsterdam: IOS Press) p 751
[16] Perali A, Pieri P, Strinati G C and Castellani C 2002 *Phys. Rev.* B **66** 024510
[17] Randeria M 1995 *Bose Einstein Condensation* ed A Griffin *et al* (Cambridge: Cambridge University Press) pp 355–92
[18] Hufner S, Hossain M A, Damascelli A and Sawatzky G 2008 *Rep. Prog. Phys.* **71** 062501
[19] Leggett A J 2006 *Nature Phys.* **2** 134
[20] Emery V J and Kivelson S A 1995 *Nature* **374** 434
[21] Anderson P W, Lee P A, Randeria M, Rice T M, Trivedi N and Zhang F C 2004 *J. Phys.: Condens. Matter.* **16** R755
[22] Lee P A, Nagaosa N and Wen X G 2006 *Rev. Mod. Phys.* **78** 17
[23] Levin K, Chen Q J, Chien C-C and He Y 2008 arXiv:0810.1938
[24] Georges A 2007 *Ultra-cold Fermi Gases* ed M Inguscio *et al* (Amsterdam: IOS Press) p 477
[25] Thomas J E, Kinast J and Turlapov A 2005 *Phys. Rev. Lett.* **95** 120402
[26] Ketterle W and Zwierlein M W 2007 *Ultra-cold Fermi Gases* ed M Inguscio *et al* (Amsterdam: IOS Press) p 95
[27] Stewart J T, Gaebler J P and Jin D S 2008 *Nature* **454** 744
[28] Damascelli R, Hussain Z and Shen Z-X 2003 *Rev. Mod. Phys.* **75** 473
[29] Campuzano J C, Norman M R and Randeria M 2004 Photoemission in the high T_c superconductors *Physics of Superconductors* (Berlin: Springer) vol 2 pp 167–273
[30] Norman M R and Pepin C 2003 *Rep. Prog. Phys.* **66** 1547

[31] Schunck C, Shin Y-I, Schirotzek A and Ketterle W 2008 *Nature* **454** 739
[32] Partridge G B, Li W, Kamar R I, Liao Y A and Hulet R G 2006 *Science* **311** 503
[33] Partridge G B, Li W, Liao Y A, Hulet R G, Haque M and Stoof H T C 2006 *Phys. Rev. Lett.* **97** 190407
[34] Shin Y, Zwierlein M W, Schunck C H, Schirotzek A and Ketterle W 2006 *Phys. Rev. Lett.* **97** 030401
[35] Zwierlein M W, Schirotzek A, Schunck C H and Ketterle W 2006 *Science* **311** 492
[36] Fulde P and Ferrell R A 1964 *Phys. Rev.* **135** A550
Larkin A I and Ovchinnikov Y N 1964 *Zh. Eksp. Teor. Fiz.* **47** 1136
Larkin A I and Ovchinnikov Y N 1965 *Sov. Phys.—JETP* **20** 762
[37] Dao T L, Georges A, Dalibard J, Salomon C and Carusotto I 2007 *Phys. Rev. Lett.* **98** 240402
[38] Törmä P and Zoller P 2000 *Phys. Rev. Lett.* **85** 487
[39] Bruun G M, Torma P, Rodriguez M and Zoller P 2001 *Phys. Rev.* A **64** 033609
[40] Stajic J, Milstein J N, Chen Q J, Chiofalo M L, Holland M J and Levin K 2004 *Phys. Rev.* A **69** 063610
[41] Kinnunen J, Rodriguez M and Törmä P 2004 *Phys. Rev. Lett.* **92** 230403
[42] Chin C, Bartenstein M, Altmeyer A, Riedl S, Jochim S, Denschlag J H and Grimm R 2004 *Science* **305** 1128
[43] Kinnunen J, Rodriguez M and Törmä P 2004 *Science* **305** 1131
[44] Chen Q J, Levin K and Kosztin I 2001 *Phys. Rev.* B **63** 184519
[45] He Y, Chen Q J and Levin K 2005 *Phys. Rev.* A **72** 011602(R)
[46] Chen Q J, Stajic J and Levin K 2005 *Phys. Rev. Lett.* **95** 260405
[47] Yu Z and Baym G 2006 *Phys. Rev.* A **73** 063601
[48] Yu Z and Baym G 2006 *Phys. Rev.* A **73** 063601
Baym G, Pethick C J, Yu Z and Zwierlein M W 2007 *Phys. Rev. Lett.* **99** 190407
[49] Shin Y, Schunck C H, Schirotzek A and Ketterle W 2007 *Phys. Rev. Lett* **99** 090403
[50] Perali A, Pieri P and Strinati G C 2008 *Phys. Rev. Lett.* **100** 010402
[51] Basu S and Mueller E 2008 *Phys. Rev. Lett.* **101** 060405
[52] He Y, Chien C C, Chen Q J and Levin K 2009 *Phys. Rev. Lett.* **102** 020402
[53] He Y, Chien C-C, Chen Q J and Levin K 2008 *Phys. Rev.* A **77** 011602(R)
[54] Massignan P, Bruun G M and Stoof H T C 2008 *Phys. Rev.* A **77** 031601(R)
[55] Sheehy D E and Radzihovsky L 2006 *Phys. Rev. Lett.* **96** 060401
[56] De Silva T N and Mueller E J 2006 *Phys. Rev.* A **73** 051602(R)
[57] Chien C-C, Chen Q J, He Y and Levin K 2006 *Phys. Rev. Lett.* **97** 090402
[58] Chien C-C, Chen Q J, He Y and Levin K 2007 *Phys. Rev. Lett.* **98** 110404
[59] Kinnunen J, Jensen L M and Törmä P 2006 *Phys. Rev. Lett.* **96** 110403
[60] Schunck C H, Shin Y, Schirotzek A, Zwierlein M W and Ketterle W 2007 *Science* **316** 867
[61] Lobo C, Recati A, Giorgini S and Stringari S 2006 *Phys. Rev. Lett.* **97** 200403
[62] Combescot R, Recati A, Lobo C and Chevy F 2007 *Phys. Rev. Lett.* **98** 180402
[63] Punk M and Zwerger W 2007 *Phys. Rev. Lett.* **99** 170404
[64] Schirotzek A, Shin Y, Schunck C H and Ketterle W 2008 *Phys. Rev. Lett.* **101** 140403
[65] Ding H, Yokoya T, Campuzano J C, Takahashi T, Randeria M, Norman M R, Mochiku T, Hadowaki K and Giapintzakis J 1996 *Nature* **382** 51
[66] Chen Q J, Kosztin I, Jankó B and Levin K 1999 *Phys. Rev.* B **59** 7083
[67] Chien C-C, He Y, Chen Q J and Levin K 2008 *Phys. Rev.* A **77** 011601
[68] Micnas R 2007 *Phys. Rev.* B **76** 184507
[69] Micnas R, Ranninger J and Robaszkiewicz S 1990 *Rev. Mod. Phys.* **62** 113
[70] Nozières P and Schmitt-Rink S 1985 *J. Low Temp. Phys.* **59** 195
[71] Chien C C, Chen Q J and Levin K 2008 *Phys. Rev.* A **78** 043612
[72] Pieri P, Pisani L and Strinati G C 2004 *Phys. Rev.* B **70** 094508
Haussmann R, Rantner W, Cerrito S and Zwerger W 2007 *Phys. Rev.* A **75** 023610
Fukushima N, Ohashi Y, Taylor E and Griffin A 2007 *Phys. Rev.* A **75** 033609
Hu H, Drummond P D and Liu X J 2007 *Nature Phys.* **3** 469
[73] Andersen J O 2004 *Rev. Mod. Phys* **76** 599
[74] Maly J, Jankó B and Levin K 1999 *Physica* C **321** 113
[75] Kosztin I, Chen Q J, Jankó B and Levin K 1998 *Phys. Rev.* B **58** R5936
[76] Jankó B, Maly J and Levin K 1997 *Phys. Rev.* B **56** R11407
[77] Chen Q J, Yan H, Chien C-C and Levin K 2007 *Phys. Rev.* B **75** 014521
[78] Norman M R, Kanigel A, Randeria M, Chatterjee U and Campuzano J C 2007 *Phys. Rev.* B **76** 174501
[79] Chubukov A V, Norman M R, Millis A J and Abrahams E 2007 *Phys. Rev.* B **76** 180501(R)
[80] Maly J, Jankó B and Levin K 1999 *Phys. Rev.* B **59** 1354
[81] Chen Q J and Levin K 2008 *Phys. Rev.* B **78** 020513(R)
[82] Chen Q J, Kosztin I, Jankó B and Levin K 1998 *Phys. Rev. Lett.* **81** 4708
[83] Perali A, Pieri P, Pisani L and Strinati G C 2004 *Phys. Rev. Lett.* **92** 220404
[84] Shin Y I, Schunck C H, Schirotzek A and Ketterle W 2008 *Nature* **451** 689
[85] Chen Q J and Levin K 2009 *Phys. Rev. Lett.* **102** 020402
[86] Kanigel A, Chatterjee U, Randeria M, Norman M R, Souma S, Shi M, Li Z Z, Raffy H and Campuzano J C 2007 *Phys. Rev. Lett.* **99** 157001
[87] Kanigel A *et al* 2006 *Nature Phys.* **2** 447
[88] Lee W S, Vishik I M, Tanaka K, Lu D H, Sasagawa T, Nagaosa N, Devereaux T P, Hussain Z and Shen Z X 2007 *Nature* **450** 81
[89] Kohsaka Y *et al* 2008 *Nature* **454** 1072